The Magnetic Resonance Force Microscope

P. Chris Hammel and Denis V. Pelekhov
Ohio State University, Columbus, OH, USA

1 INTRODUCTION

The emerging technique of magnetic resonance force microscopy (MRFM) (Sidles, 1991) was conceived by Sidles (1992) as a tool that could provide the revolutionary capability for three-dimensional imaging of single-copy biomolecules. This challenging goal has been augmented by a growing interest in applying it to imaging, especially subsurface imaging, of a broad range of materials and devices including those that are the subject of this handbook.

New materials and devices with unprecedented capabilities and levels of performance are being created by tailoring the structure and composition of multicomponent materials at the nanometer scale. Some of the most important examples are systems incorporating and exploiting electronic spin in its many manifestations including ferromagnetism. A central component of a successful materials development program is the availability of characterization tools. Progress in the development of spin electronics materials and devices will depend on tools capable of providing detailed microscopic information about the electronic, magnetic, and structural properties of these materials systems. In addition to studying the constituents of these systems the ability to image and characterize buried interfaces in multicomponent systems is a particularly important requirement.

The MRFM is a novel scanned-probe instrument which combines the three-dimensional imaging capabilities of magnetic resonance imaging (MRI) with the high sensitivity and resolution of atomic force microscopy. It will enable nondestructive, chemical-specific, high-resolution microscopic studies and imaging of *subsurface* properties of a broad range of materials. Dramatic improvements in the capabilities of the MRFM in the last decade have confirmed the validity of the approach in nuclear magnetic resonance (NMR) (Rugar *et al*., 1994), electron spin resonance (ESR) (Rugar, Yannoni and Sidles, 1992; Hammel, Zhang, Moore and Roukes, 1995; Bruland *et al*., 1998) and ferromagnetic resonance (FMR) experiments (Zhang, Hammel and Wigen, 1996; Wago, Botkin, Yannoni and Rugar, 1998; Zhang *et al*., 1998; Hammel, Zhang and Midzor, 1998). In the quest for improved sensitivity a recent milestone – the detection of a single electronic spin using by MRFM – has been demonstrated by the IBM group (Rugar, Budakian, Mamin and Chui, 2004). Several good reviews are available (Sidles *et al*., 1995; Yannoni, Züger, Rugar and Sidles, 1996; Pelekhov *et al*., 2002; Wigen, Roukes and Hammel, 2006).

Because spatial resolution in MRI is limited by the requirement that adequate signal (compared to detection noise) be obtained from the resolved volume, this breakthrough heralds new horizons in magnetic resonance imaging. This is a unique accomplishment amongst single spin detectors in that MRFM couples directly to the electron's magnetic

Handbook of Magnetism and Advanced Magnetic Materials. Edited by Helmut Kronmüller and Stuart Parkin. Volume 5: *Spintronics and Magnetoelectronics*. ISBN: 978-0-470-02217-7.

dipole moment. Other high sensitivity approaches exploit mechanisms that couple the spin of the electron to its spatial degrees of freedom, hence allowing the spin to be detected through its coupling to the electronic charge. The much larger interaction force afforded by coupling to the charge carries the limitations associated with the particular environment required to obtain the needed interaction between the electron spin and orbital degrees of freedom. MRFM is a general technique applicable wherever conventional magnetic resonance would apply, this generality of applicability is a central strength of the MRFM.

The development of MRFM instruments capable of fulfilling these goals will be built on techniques that improve sensitivity and overcome the challenges inevitable in applying them under various the experimental conditions these applications entail. In this chapter, we focus on these two aspects of MRFM: Sections 2–4 discuss the fundamentals of the technique and the various components of a microscope, and in Section 5 several applications to problems will be discussed.

2 UNDERLYING TECHNOLOGIES

2.1 Magnetic resonance

2.1.1 Fundamentals

Electrons and many atomic nuclei possess a magnetic moment μ. This moment is related their spin angular momentum J by the gyromagnetic ratio γ which is unique for each moment

$$\boldsymbol{\mu} = \gamma \mathbf{J} \tag{1}$$

The electronic moment $\mu_e = 9.28 \times 10^{-24}\,\mathrm{J\,T^{-1}} \approx \mu_\mathrm{B}$ is approximately 10^3 times larger than nuclear moments. Because spin moments possess both magnetic moment and angular momentum, the torque exerted by an external magnetic field H results in precession of the moment about the field:

$$\frac{\mathrm{d}\boldsymbol{\mu}}{\mathrm{d}t} = \boldsymbol{\mu} \times \gamma \mathbf{H} \tag{2}$$

The precession frequency (the Larmor frequency) is $\omega_\mathrm{L} = \gamma H$.

A magnetic moment in a magnetic field H exhibits a resonant response to a transverse magnetic field H_1 oscillating at frequency ω_L. This effect emerges in a simple quantum mechanical as well as classical picture. The Hamiltonian for a magnetic moment in a magnetic field H applied along the $\hat{z}$ direction, is

$$\mathcal{H} = -\boldsymbol{\mu} \cdot \mathbf{H} \tag{3}$$

hence,

$$E_m = -\gamma \hbar H m \tag{4}$$

where $m = J, J-1, \ldots, -J+1, -J$ is the projection of the spin angular momentum $\mathbf{J}$ along the field axis $\mathbf{H}$. Therefore the energy of the transition between states having initial and final spin projections m_i and m_f is

$$\Delta E = -\gamma \hbar H \Delta m \tag{5}$$

where $\Delta m = m_f - m_i$. The transition is stimulated by a transverse oscillating field $H_1 = H_1 \hat{x} \cos(\omega t)$. The matrix element for this perturbation is

$$\left\langle m_f \left| -\gamma \hbar H_1 J_x \right| m_i \right\rangle \tag{6}$$

Writing $J_x = (1/2)(J_+ + J_-)$ we see it is nonzero only for $\Delta m = \pm 1$. Thus the energy of the allowed resonant transitions is

$$|\Delta E| = \gamma \hbar H = \hbar \omega_\mathrm{L} \tag{7}$$

and therefore energy is absorbed at the resonant excitation frequency $\omega_\mathrm{L} = \gamma H$.

2.1.2 Spin susceptibility

The spin polarization of an ensemble of N particles of spin J in thermal equilibrium at temperature T with a magnetic field of magnitude H_0 is governed by Boltzmann statistics (Abragam, 1961). The populations of energy levels of the spin system are proportional to $\exp(-E_m/k_\mathrm{B}T)$. The net equilibrium magnetization M of the ensemble is

$$M = N\gamma\hbar \frac{\sum_{m=-J}^{J} m \exp(-E_m/k_\mathrm{B}T)}{\sum_{m=-J}^{J} \exp(-E_m/k_\mathrm{B}T)} \tag{8}$$

Exploiting the high-temperature approximation (usually an excellent approximation) $E_m/k_\mathrm{B}T \ll 1$ we obtain the following expression for M and the spin susceptibility $\chi_0 = M/H_0$:

$$M = \frac{N\gamma^2\hbar^2 J(J+1)}{3k_\mathrm{B}T} H_0 = \chi_0 H_0 \tag{9}$$

2.1.3 Spin relaxation

A spin system that is removed from this thermal equilibrium state will regain it through interactions with its environment, a thermal reservoir, typically the crystal lattice hosting the spin, at temperature T. This process requires transitions between spin states, and these

require fluctuating magnetic fields analogous to the field H_1 described in Section 2.1.1 above. These fields must fluctuate at ω_L and have a component oriented perpendicular to the direction of the polarizing magnetic field H_0. The time evolution of ensemble magnetization M is given by

$$\frac{dM_z}{dt} = -\frac{M_z - M_0}{T_1} \tag{10}$$

where T_1 is the longitudinal spin relaxation time that is determined by the intensity of fluctuations of the transverse local field at the frequency $\omega_L = \gamma H_0$. It describes the process of realigning the spin with the direction of polarizing magnetic field. It can be expressed (Abragam, 1961) in terms of the transverse fluctuating fields $H_\pm$ capable of driving $\Delta m = \pm 1$ transitions between $|m\rangle$ states:

$$\frac{1}{T_1} = \gamma^2 \int_{-\infty}^{\infty} \langle H_\pm(0) H_\pm(\tau)\rangle e^{i\gamma H_0 \tau} d\tau \tag{11}$$

The integral is the spectral density $J_\pm$ of the field fluctuations, given by the Fourier transform of the time autocorrelation function of the field fluctuations, and it describes the intensity of these fluctuations at frequency ω:

$$J_\pm(\omega) = \int_{-\infty}^{\infty} \langle H_\pm(0) H_\pm(\tau)\rangle e^{i\omega\tau} d\tau \tag{12}$$

Hence we see that the rate at which spins relax is proportional to this spectral density evaluated at the Larmor frequency, that is, those fluctuating fields capable of causing $\Delta m = \pm 1$ transitions.

A monochromatic transverse field H_1 can coherently rotate M_z into the $\hat{x}-\hat{y}$ plane thus generating a transverse magnetization M_x and M_y; this magnetization will subsequently decay for two reasons. Inhomogeneous relaxation results if different spins experience different magnetizing fields due to spatial inhomogeneity. Different spins will precess at different frequencies causing loss of coherence and eventually loss of the transverse magnetization. A Lorentzian distribution of fields with a half-width ΔH will decohere the transverse magnetization on a timescale:

$$T_2^* = (\gamma \Delta H)^{-1} \tag{13}$$

Interactions between nuclear spins also cause decoherence of the transverse magnetization; these are described by transverse spin relaxation time T_2: (Abragam, 1961)

$$\frac{dM_x}{dt} = -\frac{M_x}{T_2}, \frac{dM_y}{dt} = -\frac{M_y}{T_2} \tag{14}$$

2.1.4 Rotating frame of reference

It is helpful in understanding the dynamics of spins simultaneously experiencing static and oscillating transverse fields to apply a simple transformation (Slichter, 1989) into a frame of reference that rotates about the axis defined by the applied field $\mathbf{H}_0$ (typically $\hat{z}$). The linearly polarized transverse oscillating rf field $H_x = 2H_1 \cos(\omega_{rf} t)$ that is applied in magnetic resonance can be written as a superposition of two oppositely circularly polarized fields of amplitude H_1 rotating with frequencies $\pm\omega_{rf}$ (Abragam, 1961). In practice, only one of the circularly polarized components need be considered since the counter-rotating component is far off resonance ($2\omega_{rf}$) and has little effect on the spin system. In a frame rotating at ω_{rf} the first oscillating field is static, so the magnetic field seen by a spin (see Figure 1) is given by:

$$\mathbf{H}_{eff} = \left(H_z^{tot} - \frac{\omega_{rf}}{\gamma}\right)\hat{z} + H_1\hat{x} \tag{15}$$

Here $H_z^{tot} = H_0 + H_z^{tip}$ to explicitly allow for the fact that in MRFM the field of the micromagnetic tip H_{tip} adds to the field experienced by the sample. In the rotating frame, the resonance condition leads to a particularly simple situation:

$$\frac{\Delta\omega}{\gamma} = H_z^{tot} - \frac{\omega_{rf}}{\gamma} = 0 \Rightarrow \mathbf{H}_{eff} = H_1\hat{x} \tag{16}$$

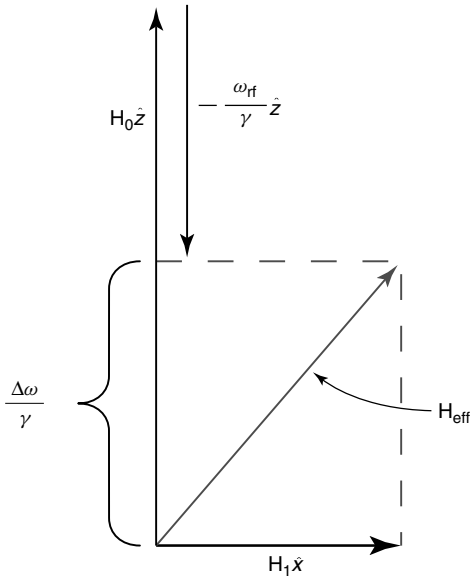

Figure 1. Diagram of magnetic fields in a frame of reference rotating about $\hat{\mathbf{z}}$ with angular frequency ω_{rf}. The resulting effective field $\mathbf{H}_{eff}$ is the vector sum of the applied magnetic field $\mathbf{H}_0$, the transverse field $\mathbf{H}_1$ and the field $-(\omega_{rf}/\gamma)\hat{z}$ that accounts for the transformation to the rotating frame of reference.

Hence the magnetization precesses about $H_1\hat{x}$ at a frequency γH_1, the Rabi frequency. The $\hat{x}$ component of H^{tip} is static and much less than H_0, so it can be neglected.

2.1.5 The Bloch equations

The equations of motion (equation (2)) for the magnetization **M** can be written in the rotating frame of reference including longitudinal and transverse spin relaxation as

$$\frac{\mathrm{d}\mathbf{M}}{\mathrm{d}t} = \gamma\,(\mathbf{M} \times \mathbf{H}_{\text{eff}}) - \frac{M_x\hat{x} + M_y\hat{y}}{T_2} - \frac{M_z - M_0}{T_1}\hat{z} \quad (17)$$

The steady-state solutions of these, the well-known Bloch equations (Bloch, 1946; Abragam, 1961), are

$$M_x = \frac{\Delta\omega\gamma H_1 T_2^2}{1 + (T_2\Delta\omega)^2 + \gamma^2 H_1^2 T_1 T_2} M_0 \quad (18)$$

$$M_y = \frac{\gamma H_1 T_2}{1 + (T_2\Delta\omega)^2 + \gamma^2 H_1^2 T_1 T_2} M_0 \quad (19)$$

$$M_z = \frac{1 + (\Delta\omega T_2)^2}{1 + (T_2\Delta\omega)^2 + \gamma^2 H_1^2 T_1 T_2} M_0 \quad (20)$$

where $\Delta\omega = \omega_{\text{rf}} - \omega_{\text{L}}$. The frequency dependence of $M_z(\omega)$, related to the magnetic resonance lineshape, is a (negative-going) Lorentzian whose minimum occurs at $\Delta\omega = 0$. The linewidth, or full width at half intensity, $\delta\omega$ is

$$\delta\omega = 2\frac{\sqrt{1 + \gamma^2 H_1^2 T_1 T_2}}{T_2} \quad (21)$$

2.2 Magnetic resonance imaging

Magnetic resonance imaging (MRI) is a large and rich field that employs an applied magnetic field gradient to map the spatial location of a particular volume onto either the frequency or the applied homogeneous field of a detected magnetic resonance signal. The relationship between the frequency ω_{L} of a spin and the magnetic field H it experiences is

$$\omega_{\text{L}} = \gamma H \quad (22)$$

A magnetic field gradient applied along the $\hat{z}$ direction $\mathrm{d}H/\mathrm{d}z$ creates a spatial distribution of spin resonant frequencies:

$$\omega_{\text{L}}(z) = \gamma\left(H_0 + \frac{\mathrm{d}H_z}{\mathrm{d}z}z\right) \quad (23)$$

Conventional MRI (Callaghan, 1991) employs pulsed magnetic resonance techniques that produce a time-domain spin echo signal. This signal will decay rapidly as a consequence of the broad range of fields present, that is, it will exhibit a short T_2^* (see equation (13)). The Fourier transform of this time-domain decay will produce spectrum in which the signal intensity at a particular frequency corresponds to the number spins at the z-coordinate prescribed by the field gradient.

Alternatively, one can employ monochromatic rf radiation of frequency ω_{rf}, then only those spins lying on a surface of constant field (perpendicular to the field gradient) at z_{res} will contribute to the signal:

$$z_{\text{res}} = \frac{\left(\frac{\omega_{\text{rf}}}{\gamma} - H_0\right)}{\frac{\mathrm{d}H_z}{\mathrm{d}z}} \quad (24)$$

The thickness δz of the resonance volume is determined by the *homogeneous* linewidth of the sample $(\gamma T_2)^{-1}$

$$\delta z = \frac{(\gamma T_2)^{-1}}{\frac{\mathrm{d}H_z}{\mathrm{d}z}} \quad (25)$$

This width determines the spatial resolution of MRI.

The resolution of MRI is limited by detection sensitivity and the requirement that the resolved volume be large enough to provide acceptable signal-to-noise ratio. Pulsed MRI protocols employ pulsed spatial field gradients applied along three orthogonal directions combined with rf pulses to assign a unique value of spin precession frequency and phase to spins within a resolved region having volume $(\delta z)^3$. We see from equation (25) that spatial resolution can be improved by increasing the field gradient strengths. This improvement comes at the price of diminished signal which is proportional to the number of spins $N_{\text{spins}} = n(\delta z)^3$ in the volume element (n is the spin density). Conventional spectrometers can detect the signal from 10^9 electron spins ($\sim 10^{15}$ nuclear spins) in bandwidths of order 1 Hz. The finest spatial resolution reported in inductively detected nuclear micro-MRI is at the level of $(\sim 3\,\mu\text{m})^3$ (Ciobanu, Seeber and Pennington, 2002).

2.3 Scanned-probe microscopy

Scanned-probe microscopy (SPM) refers to a large family of experimental techniques based on detection of a local interaction between a sample and a microscale probe that can be precisely positioned over the sample. Raster scanning of the microprobe over the sample surface provides a spatial map of the detected interaction.

2.3.1 Scanning tunneling microscopy

The first scanned-probe microscope was the scanning tunneling microscope (STM) invented by Gerd Binnig and Heini Rohrer in 1982. In this instrument an atomically sharp

conducting needle is brought close to conducting surface, close enough for electrons tunnel through the vacuum gap (typically $\sim$1 Å) between the tip and the surface in the presence of a potential difference. The extremely short range of the tunneling interaction allows mapping of the local density of electronic states with atomic scale resolution. Mapping of surface topography, local state spectroscopy, and atomic manipulation have all been accomplished with the STM. The STM is, however, limited to conducting surfaces.

2.3.2 Atomic force microscopy

The atomic force microscope (AFM) uses as a probe a flexible micromechanical cantilever with a sharp tip. The interaction between this probe and the surface is detected by measuring the resulting displacement of the cantilever. The typical magnitude of the forces involved is 10^{-9}–10^{-12} N. The displacement of the cantilever is measured using optical displacement detection. The AFM can operate on insulating as well as conducting surfaces, and also provides information about the surface of the sample. AFM can be used for mapping surface topography, stiffness, local friction, and for surface manipulation. It is usually operated in one of two modes: contact mode and noncontact mode. In contact mode the cantilever is in hard contact with the surface and the displacement of the cantilever under the influence of the force of Pauli repulsion is measured. In noncontact mode, an oscillating cantilever hovers above the sample surface and the local gradient of the long-range dipolar (Van der Waals) force is measured by detecting the consequent shift of the natural frequency of the cantilever ω_c. The spatial resolution of AFM is defined, depending on the mode of operation, by parameters such as the radius of the cantilever tip (typically $\sim$10 nm) and the probe–sample separation. Under proper conditions atomic resolution is achievable (Giessibl, 2003).

2.3.3 Magnetic force microscope

The magnetic force microscope (MFM) is a form of AFM that detects the dipolar magnetostatic interaction between the magnetic tip and magnetic dipoles in a ferromagnetic sample. The tip is scanned at a controlled distance above the sample without direct contact. The typical probe–sample interaction has similar magnitude: 10^{-9}–10^{-12} N.

3 THE MRFM INSTRUMENT

MRFM is similar to MFM; the essential difference is the addition of an applied rf field to enable the sample magnetization to be manipulated by magnetic resonance techniques. Because the goal is high spatial resolution imaging, the signal detected is, in general, from a small number of paramagnetic spins, hence the forces are much smaller than in the case of other force microscopies.

A micromechanical cantilever with a micromagnetic probe tip is brought close to the sample surface. The force F exerted on the magnetic tip by magnetic moments in the sample is

$$\mathbf{F} = -(\mathbf{m} \cdot \nabla)\mathbf{B} \tag{26}$$

where $\mathbf{m}$ is the magnetic moment of the sample and $\nabla\mathbf{B}$ is the gradient of the magnetic field of the micromagnetic tip. This force will deflect the compliant cantilever; sensitive displacement detection allows this force to be measured. Using magnetic resonance techniques, the sample magnetization is manipulated at or near the resonant frequency ω_c of the cantilever. The amplitude of the cantilever response is multiplied by Q thus reducing the demands on the displacement detection. Forces as small as 10^{-18} N have been detected (Hoen *et al*., 1994). MRFM can be applied for detection of any kind of magnetic resonance: ESR, NMR, and FMR. Force detection of magnetic resonance detection is far more sensitive than conventional inductive detection, and recently Rugar and coworkers demonstrated MRFM detection of a single electron spin (Rugar, Budakian, Mamin and Chui, 2004). By comparison, the sensitivity of a commercially available inductively detected ESR spectrometer is $\sim 10^9$ spins.

3.1 Micromechanical resonator

The heart of the MRFM is the resonant micromechanical force sensor. The most commonly used structure is a micromechanical beam of length L, width W and thickness T typically clamped at one end, that is, configured as a cantilever, though doubly clamped is also feasible. Other structures such as torsional oscillators (Barrett *et al*., 1998) have also been used for MRFM force detection however, cantilevers are by far more popular and we will focus on them here. MRFM cantilevers with characteristic dimensions $L \approx 300$–$500\,\mu$m, $W \approx 20\,\mu$m and $T \approx 0.5\,\mu$m (see Figure 2) can be fabricated by standard surface micromachining techniques (Madou, 2002). Most commonly MRFM cantilevers are made from Si and Si_3N_4.

3.1.1 The cantilever as a simple harmonic oscillator

The motion of a micromechanical beam resonator is described by the Euler- Bernoulli equation

$$\frac{\partial^2}{\partial x^2}\left[EI(x)\frac{\partial^2}{\partial x^2}z(x,t)\right] + \rho A(x)\frac{\partial^2}{\partial t^2}z(x,t) = F(x,t) \tag{27}$$

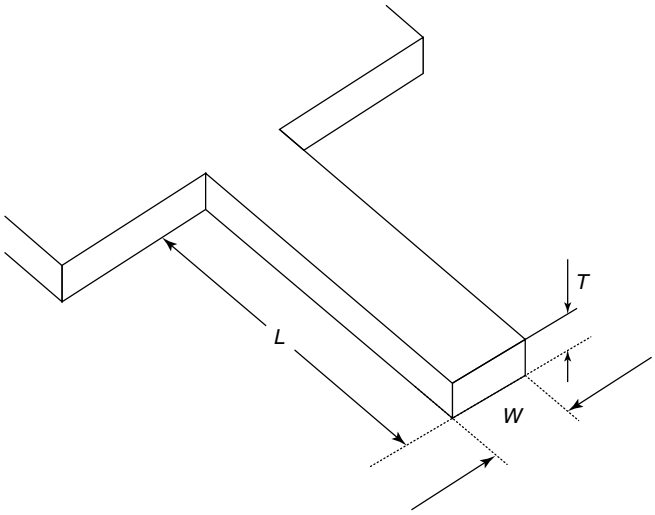

Figure 2. Schematic diagram of simple rectangular micromechanical cantilever.

where $z(x,t)$ is the transverse displacement of the beam, x is the coordinate along the beam, t is time, E is Young's modulus, ρ is the mass density, $I(x)$ is the moment of inertia about the centroid of the beam, $A(x)$ is the cross-sectional area of the beam and $F(x,t)$ is the external applied force. It can be shown that small vibrations at a coordinate x on the beam can be described by a point mass-on-spring model with effective parameters obtained from equation (27) using appropriate boundary conditions. The resulting equation of motion, with dissipation terms included, is that of a simple harmonic oscillator (SHO):

$$m\frac{\partial^2}{\partial t^2}z(t) + \frac{m\omega_c}{Q}\frac{\partial}{\partial t}z(t) + kz(t) = F(t) \tag{28}$$

where the effective parameters are the resonant frequency of the cantilever ω_c, the effective mass m of the resonator, the quality factor Q and the spring constant k of the resonator.

3.1.2 Resonator parameters

The effective parameters in equation (28) for the fundamental vibration mode are obtained from equation (27)

$$\omega_0 = a_1\sqrt{\frac{ET^2}{\rho L^4}} \tag{29}$$

$$k = a_2\frac{ET^3W}{L^3} \tag{30}$$

$$m = a_3\rho LTW \tag{31}$$

The numerical prefactors depend on x and the boundary conditions used to solve equation (27). If x corresponds to the free end of a simple rectangular cantilever (shown in Figure 2), the prefactors are $a_1 \approx 1.0$, $a_2 \approx 0.25$ and $a_3 \approx 0.25$.

3.1.3 Resonator response to oscillatory excitation

MRFM force detection exploits the response of a cantilever to an oscillatory force

$$F(t) = F_0 e^{\iota\omega t} \tag{32}$$

In the low damping approximation ($Q \gg 1$) the cantilever displacement is

$$z(\omega,t) = A_0 e^{\iota(\omega t+\theta_0)} + e^{-\frac{\omega_c}{2Q}t}\left(C_1 e^{-\iota\omega_c t} + C_2 e^{\iota\omega_c t}\right) \tag{33}$$

where

$$A_0(\omega) = \frac{F_0/m}{\sqrt{(\omega_c^2-\omega^2)^2 + (\omega_c\omega/Q)^2}} \tag{34}$$

$$\theta_0(\omega) = \arctan\left[\frac{\omega_c\omega}{Q(\omega^2-\omega_c^2)}\right] \tag{35}$$

where C_1 and C_2 are complex coefficients determined by initial conditions.

The first term of equation (33) gives the steady-state response of the cantilever. While the response of the cantilever to a static force F_0 is $A_0(0) = F_0/k$ the response to an oscillatory force of the same magnitude at $\omega = \omega_c$ is $A_0(\omega_c) = QF_0/k$, that is the oscillation amplitude is multiplied by the quality factor Q of the cantilever, typically 10^4–10^5, compared to the off-resonant response. This has the important consequence of reducing the *displacement readout* sensitivity (see Section 3.2) needed to ensure that it doesn't limit overall sensitivity.

The second term in equation (33) represents the transient response of the cantilever which decays on the oscillator response timescale

$$\tau = \frac{2Q}{\omega_c} \tag{36}$$

This reflects the fact that changing the amplitude involves changing the oscillator energy by means of the rather small signal force. When an oscillatory force is applied to an otherwise undriven resonator its oscillation amplitude will grow until a steady state is reached in which the work done by the external force (on resonance the force is in phase with the velocity, so it performs work) is balanced by the energy dissipated per cycle ($\propto Q^{-1}$). The response time τ reflects the time required to increase the energy of the resonator to this equilibrium. This time can be long for the high Q cantilevers used in MRFM: typically $Q \sim 5\times10^4$ and $\omega_0 = 2\pi\times10^4$ Hz, so $\tau \approx 1.6$ s. This slow response

can be substantially improved by the application of negative force feedback without significantly degrading the cantilever force sensitivity (Mertz, Marti and Mlynek, 1993; Bruland, Garbini, Dougherty and Sidles, 1996) if necessary.

3.2 Displacement detection

3.2.1 Optical interferometry

Optical displacement detection based on fiber-optic interferometry (Albrecht, Grütter, Rugar and Smith, 1992) is currently nearly universal in MRFM experiments. Laser light launched into one port of a directional fiber coupler (see Figure 3) propagates to the end of the fiber positioned a distance δ from the backside of the cantilever. The gap between the end of the fiber and the reflective cantilever surface forms an interferometric cavity. Cantilever motion changes this gap altering the interference between the reference beam internally reflected off the end of the fiber and the signal beam reflected off the cantilever and back into the fiber. The dependence of the light power on δ is

$$P_p \propto P_{s0} + P_{r0} + 2\sqrt{P_{s0}P_{r0}}\cos\left(\frac{4\pi}{\lambda}\delta\right) \tag{37}$$

where λ is the wavelength of the laser light and P_{s0} and P_{r0} are the powers of the signal and reference beams respectively. To maximize the displacement sensitivity $\mathrm{d}P_p/\mathrm{d}\delta$, the interferometric cavity should be tuned such that

$$\delta = \frac{\lambda}{4}\left(\frac{1}{2} \pm n\right), \quad n = 1, 2, 3 \ldots \tag{38}$$

The amplitude of the reference and the signal beams depends on the power of the laser light P_{laser} and on the reflectivity R_s of the cantilever and R_r of the end of the fiber, so the displacement sensitivity is

$$\left|\frac{\mathrm{d}P_p}{\mathrm{d}\delta}\right| = \frac{8\pi}{\lambda}P_{\mathrm{laser}}(1 - R_r)R_sR_r \tag{39}$$

The sensitivity can be optimized by tuning the reflectivity of the interferometric surfaces with a metallic coating. A displacement noise floor of $10^{-13}\,\mathrm{m\,Hz^{-1/2}}$ can be straightforwardly achieved.

3.2.2 Alternative displacement detection methods

While optical fiber interferometric displacement detection is quite popular, there are other approaches that offer advantages, for instance, in applications to photosensitive samples or where straightforward electrical readout is desired, perhaps at the expense of displacement sensitivity.

Piezoresistive

Piezoresistive displacement detection is based on measuring the change in resistance of the cantilever material resulting from stress induced by cantilever displacement. This approach has been implemented (Arlett *et al.*, 2006) with good sensitivity in Si cantilevers supported by two thin legs with a thin piezoresistive (p^+ Si) top layer. The p^+ layer forms a continuous current path through the legs, and bending will induce a stress σ leading to a change ΔR in the resistance of this path. This can in turn be related to displacement Δz of the end of the cantilever:

$$D \equiv \frac{\Delta R}{R}\frac{1}{\Delta z} = \frac{\Pi_{\mathrm{eff}}\sigma}{\Delta z} = \Pi_{\mathrm{eff}}\frac{3}{2}E\frac{h}{L^2}\left(1 - \frac{\lambda}{2L}\right) \tag{40}$$

where Π_{eff} is the effective piezoresistive coefficient of the material, E is Young's modulus, L is the length of the cantilever, h is its thickness and λ is the length of the piezoresistive region.

The minimum detectable displacement δz_{min} of the cantilever, limited by the Johnson noise in the resistor and $1/f$ noise (Yu *et al.*, 2001), is

$$\delta z_{\mathrm{min}} = \frac{4}{DV}\left[\frac{\alpha V^2}{N}\ln\frac{f_1}{f_2} + 4k_{\mathrm{B}}TR(f_1 - f_2)\right]^{1/2} \tag{41}$$

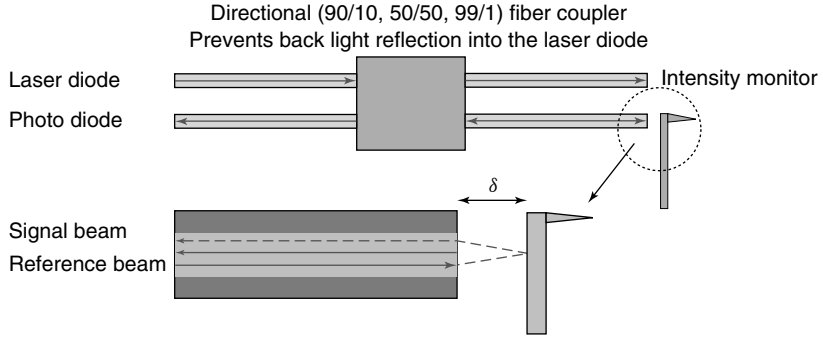

Figure 3. Schematic diagram of the optical fiber interferometer. δ is the distance between the end of the fiber and the cantilever.

where V is the bias voltage, α the $1/f$ noise parameter, N the number of carriers and f_1 and f_2 the upper and the lower limits of the measurement bandwidth. The typical displacement noise floor reported with piezoresistive cantilevers is of the order of $10^{-11}\,\mathrm{m\,Hz^{-1/2}}$ at room temperature. Experimental force sensitivities of $235\,\mathrm{aN\,Hz^{-1/2}}$ and $17\,\mathrm{aN\,Hz^{-1/2}}$ have been obtained at room temperature and 4.2 K, respectively (Arlett *et al*., 2006); optimal performance was obtained at an excitation current that balanced the opposing influences of readout noise and self heating.

Though this detection scheme has yet to be used in MRFM experiments, an integrated piezoresistive displacement detector offers the advantage that there is no need for precision alignment of the cantilever with the detector. This step can be time consuming and its elimination could simplify MRFM experiments and hasten the dissemination of MRFM techniques to a broad research community.

Capacitive displacement detection using a microwave tank circuit

The capacitance between two electrodes varies with separation, so the displacement of a cantilever can be detected by measuring the capacitance C_p between the micromechanical resonator and a sensing electrode. Assuming small cantilever displacements, the corresponding change of the capacitance δC_p is

$$|\delta C_p| = C_p \frac{\delta d}{d} = \epsilon\epsilon_0 \frac{A}{d}\frac{\delta d}{d} \tag{42}$$

where A is the area of capacitor plates, d the distance between the plates and δd is the displacement of the resonator.

When added in parallel to the capacitance of a microwave tank circuit, C_p will lead to a measurable shift in its resonance frequency ω_{res}. The analysis of the noise performance of a tank circuit is identical to that of an SHO. The minimum detectable displacement (Pelekhov *et al*., 2005) depends on temperature T and the quality factor Q of the tank circuit. Capacitive displacement detection promises extremely high displacement detection sensitivity. For typical cantilever parameters we can expect a displacement noise floor of $10^{-13}\,\mathrm{m\,Hz^{-1/2}}$ at room temperature. Because the signal depends on the area of the electrode on the cantilever, this approach does not scale well as cantilevers become smaller.

This method has been used for MRFM signal detection (Pelekhov *et al*., 2005) but self heating of the tank circuit by the drive was evident at low temperatures. The tradeoff between displacement sensitivity and self heating can be helped by lithographic integration of the detection circuit with the cantilever.

Capacitive displacement detection using a single electron transistor

Another approach to capacitive displacement detection (LaHaye, Buu, Camarota and Schwab, 2004) exploits the excellent charge sensitivity of the radio frequency single electron transistor (rf SET) (Devoret and Schoelkopf, 2000). The SET is a superconducting island coupled to drain and source contacts through two tunnel junctions. The conductivity and hence the impedance of the SET arises from the tunneling of individual electrons through the tunnel contacts, and is very sensitive to the alignment of the chemical potential of the drain and source contacts. Slight changes of the island potential are evident in the SET conductance. A microwave tank circuit is used to match a room temperature detector to the impedance of the SET. On resonance, the impedance of the tank circuit is small and therefore the reflectance of the circuit is determined by the differential resistance R_d of the SET. This enables continuous, sensitive readout of the SET impedance.

When the cantilever is voltage biased and capacitively coupled to the SET, its displacement will modify R_d and hence the reflected rf power. At the low temperatures (below 300 mK) where the SET is typically operated its displacement noise is dominated by the tunnel current shot noise and the back action noise of the SET on the cantilever (LaHaye, Buu, Camarota and Schwab, 2004; Zhang and Blencowe, 2001). Theoretical estimates predict a displacement noise floor as low as $10^{-16}\,\mathrm{m\,Hz^{-1/2}}$; in the lab $3.8 \times 10^{-15}\,\mathrm{m\,Hz^{-1/2}}$ has been demonstrated using a 20 MHz beam resonator (LaHaye, Buu, Camarota and Schwab, 2004). Although it requires ultralow temperatures and has only been applied to doubly clamped beams to date, SET displacement detection is currently the most sensitive available.

3.3 Radio frequency magnetic fields

A fundamental requirement for MRFM is the transverse rf magnetic field used to manipulate the sample magnetization. The quality of the resulting force signal depends sensitively on the strength of the transverse oscillatory magnetic field H_1 that manipulates the magnetization. Standard rf field generation techniques are difficult to apply for MRFM because its scanning probe microscope arrangement makes placement of the sample and the MRFM probe inside of an rf coil (NMR) or a microwave cavity (ESR, FMR) virtually impossible. Instead, the sample must be placed as close as possible to the microstrip resonator or a microcoil used to generate the field which must be impedance matched to the 50 Ω source impedance of the rf/microwave signal generator. The nature of the impedance matching network depends on the frequency.

In the rf regime (∼100 MHz) a standard NMR tank circuit using lumped capacitive elements works well (see, e.g., Fukushima and Roeder, 1981). The microwave field needed for ESR or FMR experiments is somewhat more involved since lumped capacitive elements become impractical at these frequencies (3–10 GHz). Design strategies based on distributed microwave structures constructed from microstriplines (50 Ω planar transmission geometry with a signal line separated from a planar ground plane by a dielectric sheet) are useful. Resonant structures are desirable to increase the field; these can be based on either resonant microstriplines or microcoils.

3.3.1 Microstrip resonator

A microstrip resonator (Wallace and Silsbee, 1991) is a section of a microstrip line whose length is half the wavelength λ of the electromagnetic wave at the desired frequency $\omega_{\rm rf}$. The rf power is delivered by a transmission line that is capacitively or inductively coupled to the conducting island. The planar nature of microstrip resonators is convenient for use in scanned-probe experiments as the sample can be placed directly on the resonator (Zhang *et al.*, 1998).

3.3.2 Microcoil

A conventional coil provides a somewhat larger H_1 since the field is a sum of contributions from several windings of the coil. The need to generate rf field in GHz regime limits the inductance of the coil and therefore its size and the number of windings. The coil can be matched to the rf source by a distributed impedance matching network (Wallace and Silsbee, 1991; Zhang *et al.*, 1998; Mamin, Budakian and Rugar, 2003). Typically, ∼250 μm diameter coils with 2–2.5 windings are used. The sample is placed outside the coil on its main axis within one coil radius of the coil to achieve reasonable H_1 intensity so alignment is more demanding than for a microstrip resonator. A normal metal coil implementation delivers 1–3 G (up to ∼9 GHz) with about 10 mW of rf power delivered to the circuit.

Superconducting circuits provide strong H_1 at low power input (Mamin, Budakian and Rugar, 2003). Using this approach, a 7 G microwave field has been demonstrated ∼100 μm from a 220 μm diameter coil with 2.5 windings using only 400 μW of applied power (Mamin, Budakian and Rugar, 2003). Low applied power is important in a cryogenic environment where the heat load must be minimized. There is, however, a significant limitation imposed by superconducting resonators: the applied static field must be well below the superconducting critical field of Nb which limits the applied field to ≈2000 G. This is sufficient for ESR experiments but limiting for NMR detection.

3.4 Micromagnetic probe tips

One of the most powerful means of increasing the tip-sample interaction (equation (45)) and hence MRFM sensitivity is to increase the magnetic field gradient of the probe tip. The component of the field gradient that generates the needed force perpendicular to the plane of the cantilever will depend on the orientation of the cantilever relative to the sample surface and on the polarization of magnetic moments in the sample. For a typical geometry (as in Figure 6) we seek to maximize $\mathrm{d}B_z/\mathrm{d}z$. In a $\sim 10^5\,\mathrm{T\,m^{-1}}$ field gradient, a single electron spin generates a force of 10^{-18} N; much higher gradients will be needed for single nuclear spin sensitivity. This will require close approach to a micromagnetic probe tip.

Although not necessarily the optimal shape, we can consider a spherical ferromagnetic micromagnet to illustrate the challenge. A sphere of radius a uniformly magnetized along $\hat{z}$ with saturation magnetization M_s will have total moment $m_0 = (4/3)\pi a^3 M_s$ (see Figure 6). The field gradient a distance z from the center of the sphere is given by

$$\frac{\mathrm{d}B_z}{\mathrm{d}z} = -6\frac{\mu_0}{4\pi}\frac{m_0}{z^4} \tag{43}$$

Here $z = a + d$, where d is the gap between the sample an the magnetic sphere. For a given operating distance d, the maximum field gradient of a spherical probe magnet is achieved for a radius $a = 3d$. Given state-of-art force detection sensitivity (Rugar, Budakian, Mamin and Chui, 2004) gradients of 10^7–$10^8\,\mathrm{T\,m^{-1}}$ will be needed for single nuclear spin detection. To obtain this from an ($\mu_0 M_s = 2.2$ T) nanosphere will require $d = 46$ nm and $a = 138$ nm ($10^7\,\mathrm{T\,m^{-1}}$) or $d = 4.6$ nm and $a = 14$ nm ($10^8\,\mathrm{T\,m^{-1}}$).

The selection of the magnetic tip goes beyond the size of magnetic particle. Depending on the goals of the experiment, which might not necessarily be a single nuclear spin detection, magnetic coercivity, material stability, ease of fabrication, and the response of the magnetic tip to applied magnetic and rf fields should be considered.

3.4.1 Tip materials

Magnetic materials available for MRFM tip fabrication can be divided into magnetically 'soft' and 'hard' magnetic materials according to their coercivity.

Typically transition metals such as Co, Fe, and Ni have low coercivity, but high saturation magnetization. Fabrication is straightforward and compatible with typical microlithographic processes. This makes soft magnets attractive fabricating magnetic tips.

Hard magnetic materials such as the rare-earth alloys $SmCo_5$, Sm_2Co_{17} and $Nd_2Fe_{14}B$ exhibit coercive fields as

high as 2–3 T. Magnetic tips fabricated out of hard magnetic materials have the advantage that they can be used in MRFM experiments where an externally applied field B_{ext} antiparallel to the orientation of the tip magnetization is desired; there are applications for which this is valuable (see Section 5).

High coercivity offers another advantage. When mounted on an oscillating cantilever in an applied magnetic field, soft magnets are dissipative (Stipe *et al*., 2001a) due to magnetic 'friction' occurring as the particle's moment rotates while trying to follow the direction of the external magnetic field. This dissipation reduces the quality factor Q of the cantilever thus reducing MRFM sensitivity.

We will see in Section 5.2.1 that a long spin lifetime is crucial for ultrasensitive MRFM detection as the noise bandwidth is set by the inverse of this lifetime. Magnetic field fluctuations arising from thermal fluctuations of the tip moment will contribute to spin relaxation in the sample (see Section 2.1.3). Magnetic materials with large magnetic anisotropy K (typically larger in hard magnetic materials) reduce this effect.

3.4.2 Tip fabrication

High coercivity tips are important for high sensitivity MRFM to minimize relaxation due to tip moment fluctuations. Micromagnetic rare-earth tips are fabricated by a two step process: first small particles of the tip material are glued to the cantilever in the presence of an applied magnetic field to orient the tip moment in the desired direction. The tip is then shaped using focused ion beam milling (FIB). This technique can generate tips with gradients exceeding $10^5\,\text{T}\,\text{m}^{-1}$ ($1\,\text{G}\,\text{nm}^{-1}$). An example is shown in Figure 4.

3.4.3 Tip characterization

Characterizing the magnetic moment and the field gradient of the micromagnetic probe tip is essential and challenging due to the very small magnitude the probe magnetic moment and the need to accurately map the spatial variation of the tip field on the scale of tens or hundreds of nanometers.

Vibrating cantilever magnetometry (Zhang and Hammel, 1999; Chabot and Moreland, 2003; Stipe *et al*., 2001b) is a convenient method uniquely capable of measuring the magnetic moment of a small ferromagnetic particle mounted on a micromechanical cantilever. This approach is sensitive to moments as small as $10^4\mu_{\text{B}}$ (Stipe *et al*., 2001b) and so is suitable for the study of nanoscale magnetic tips. The motion of a magnetic particle at the end of a cantilever entails rotation its magnetic moment with respect to the externally applied magnetic field; this leads to a restoring torque that depends on the position of the cantilever and so changes the effective cantilever spring constant. The cantilever is driven at constant amplitude its natural frequency ω_c by means of positive feedback, and the change of its frequency is measured as a function of external magnetic field. The resulting frequency shift $\Delta\omega$ (Stipe *et al*., 2001b) is

$$\Delta\omega = \omega_c \frac{m H H_k}{2kL_e^2(H + H_{\text{K}})} \tag{44}$$

where m is the magnetic moment of the particle, L_e is the effective length of the cantilever, H_k is the anisotropy field of the tip and H is the applied magnetic field. Typical cantilever magnetometry data is shown in Figure 5. The magnetic moment of the magnetic tip can be extracted from the slope of the field dependence. Parameters such as coercivity can also be extracted. Reversals of the magnetization in response to field reversal in a soft magnet are clearly evident as slope changes.

4 FORCE DETECTION OF MAGNETIC RESONANCE

At the heart of MRFM is sensitive detection of the force $\mathbf{F}$ between a magnetic tip generating a field gradient $\nabla\mathbf{B}$ and the magnetization $\mathbf{m}$ in a localized region of the sample

$$\mathbf{F} = -(\mathbf{m}\cdot\nabla)\mathbf{B} \tag{45}$$

The characteristic force scale for MRFM is 1 atto-newton ($1\ \text{aN} = 10^{-18}\,\text{N}$) set by the interaction between a single electronic moment interacting through a field gradient of $10^5\,\text{T}\,\text{m}^{-1}$ ($1\,\text{G}\,\text{nm}^{-1}$). Detecting the force exerted by a single nuclear spin will require higher field gradients and improved force sensitivity. Detecting such forces is challenging; for comparison, forces measured in conventional SPM are usually not lower than $10^{-12}\,\text{N}$.

The transduction of a force signal into a voltage involves two stages of signal detection: first the mechanical resonator converts the oscillatory force to displacement, then this displacement is detected by a position sensitive readout. Sensitive force detection then requires the following

- System noise should be minimized
  - System noise should be dominated by thermal fluctuations of the cantilever.
  - Noise spectral density and bandwidth should be minimized.
- The signal force must be comparable to or larger than the system noise (referred to the input):

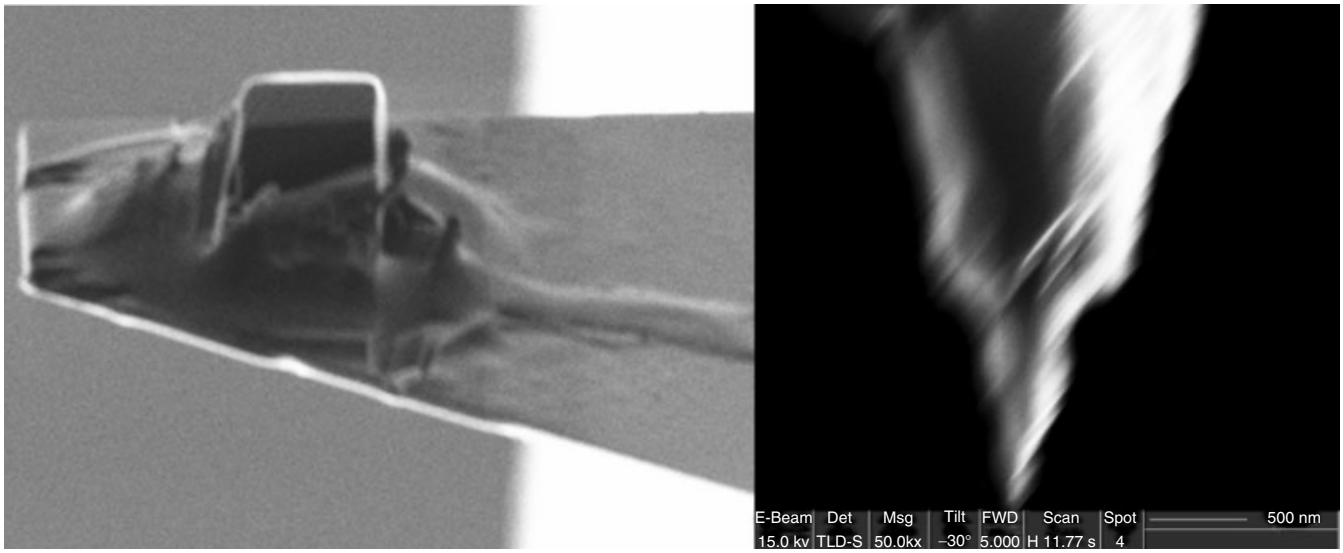

Figure 4. FIB fabricated rare-earth micromagnets (provided by P. Banerjee and R. Steward).

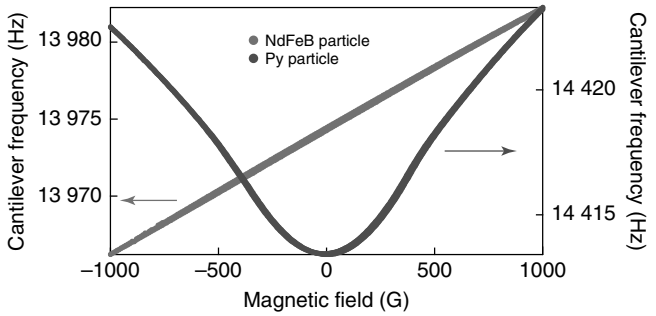

Figure 5. Cantilever magnetometry data for 'hard' NdFeB and 'soft' permalloy probe magnets. The magnetic moment of the particle can be extracted from the slope of the cantilever frequency dependence on the applied magnetic field. It can be seen that, unlike the soft-probe magnet, the hard-probe magnet preserves the direction of its magnetization as the direction of the applied field is reversed. (Provided by P. Banerjee.)

  - The field gradient should be as large as possible.
  - The force signal can be imprinted with an optimal time signature to aid detection and reject nonthermal noise.
- The noise added in reading out the resulting cantilever displacement must be negligible compared to the thermal noise of the cantilever.

This entails engineering the interaction in such a way that the resulting cantilever displacement exceeds both the cantilever displacement noise in the measurement bandwidth and the noise floor of the displacement detection scheme. The readout requirement essentially requires driving the cantilever at its resonant frequency to enhance the oscillation amplitude for a given drive.

4.1 Sensitive oscillatory force detection

The response of a cantilever to an externally applied force is well described by the model of a linear harmonic oscillator. The displacement δz of the end of a cantilever under the influence of a static force F is

$$\delta z_{\text{stat}} = \frac{F}{k} \tag{46}$$

where k is the mechanical spring constant of the cantilever. Thus, a 1 aN force acting on a soft ($k = 10^{-3}\,\text{N}\,\text{m}^{-1}$) cantilever will produce a static displacement $\delta z_{\text{stat}} = 10^{-15}$ m, well below the noise floor of available displacement detection schemes. By driving on resonance, the amplitude of the steady-state oscillations are increased by the quality factor Q:

$$\delta z_{\text{osc}} = Q\frac{F}{k} = Q\delta z_{\text{stat}} \tag{47}$$

Typically Q is $10^4 - 10^5$, resulting in an amplification of the cantilever response sufficient to render displacement readout noise negligible.

4.1.1 Fundamentals of force detection

Force sensitivity for resonant force detectors

The sensitivity of force detection using a micromechanical resonator is ultimately limited by the thermal motion δz_{th} of the resonator. By the equipartition theorem, the average thermal energy per degree of freedom of an SHO is (Albrecht,

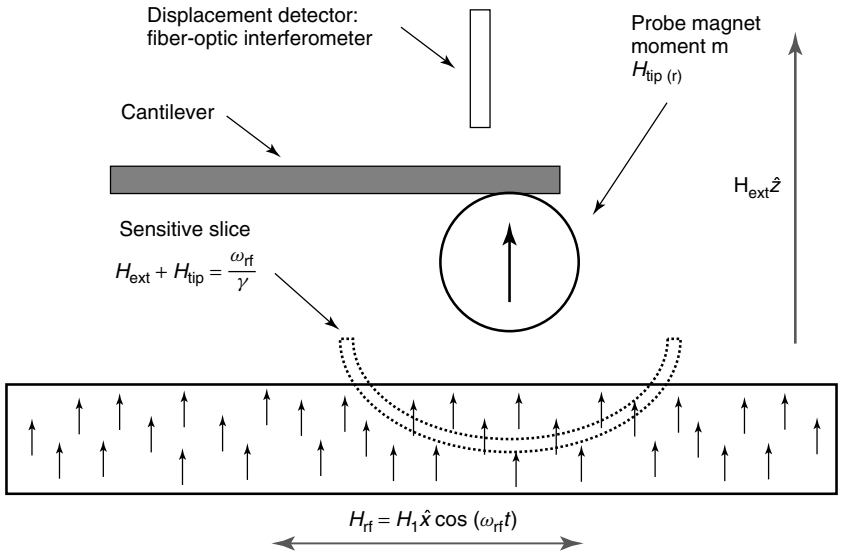

Figure 6. Schematic diagram of an MRFM experiment with probe magnet mounted on the cantilever. The cantilever is parallel to the sample surface. The sensitive slice is shown schematically.

Grutter, Horne and Rugar, 1991)

$$\frac{k\langle\delta z_{\rm th}^2\rangle}{2} = \frac{k_{\rm B}T}{2} \tag{48}$$

Equivalently we can consider the cantilever to be driven by a white noise force $F_{\rm th}$ given by (Stowe *et al.*, 1997)

$$F_{\rm th} = \sqrt{\frac{4kk_{\rm B}T\,\Delta\nu}{Q\omega_c}} \tag{49}$$

where $\Delta\nu$ is the measurement bandwidth. This expression provides a guide to the steps that can be taken to reduce $F_{\rm th}$ such as increasing Q and working at low temperature. In order to be detectable the force arising from the magnetic resonance signal should be greater than $F_{\rm th}$.

Frequency shift detection

It is often convenient, as discussed in the subsequent text, to detect the magnetic resonance signal by measuring the small induced shift in the cantilever resonance frequency ω_c. This approach requires that the cantilever be driven at its resonance frequency; we call the oscillation amplitude $z_{\rm osc}$. The fundamental limit of the sensitivity of frequency detection also arises from the thermal excitation of cantilever. The resulting thermal frequency noise $\delta\omega_{\rm th}$ is given by Albrecht, Grutter, Horne and Rugar (1991)

$$\delta\omega_{\rm th} = \sqrt{\frac{\omega_c k_{\rm B}T\,\Delta\nu}{kQ\langle z_{\rm osc}^2\rangle}} \tag{50}$$

Displacement detection sensitivity

It is important that displacement readout add negligibly to the total detection noise. A resonant oscillatory force of 10^{-18} N acting on a soft ($k = 10^{-3}\,{\rm N\,m^{-1}}$), high Q cantilever will produce cantilever oscillations $\delta z_{\rm osc} \sim 10^{-10} - 10^{-11}$ m. Hence we require displacement readout sensitivity better than $10^{-12}\,{\rm m\,Hz^{-1/2}}$. Thus, displacement sensitivity can be well managed by working at the cantilever resonance frequency.

4.1.2 Amplitude detection

Amplitude detection is the most straightforward approach to MRFM signal detection: a signal force oscillating at ω_c is applied to the cantilever, and the amplitude of the steady-state oscillations, proportional to the applied force, is measured. This approach is the most straightforward to implement and will deliver reliable results in the case of a strong magnetic resonance signal. However, amplitude detection has several disadvantages that complicate its application for high sensitivity measurements. One is the long response time τ (see equation (36) and associated discussion) required for the high Q micromechanical resonator to increase its energy and achieve its steady-state oscillation amplitude. This determines the waiting time between two consecutive signal measurements and thus the rate at which data can be acquired. For a high Q cantilever this time can be as long as 1–10 s, making acquisition of large amounts of data unacceptably time consuming. This problem can be mitigated by using negative feedback (Bruland *et al.*, 1998; Bruland, Garbini, Dougherty and Sidles, 1998) to nondissipatively increase signal bandwidth without increasing $F_{\rm th}$.

Another problem encountered in amplitude detection is the sensitivity of the cantilever frequency to conditions such as the applied field and temperature. This leads to a mismatch between the signal frequency and ω_c thus introducing a spurious variation in the oscillation amplitude that can obscure the desired signal. This is more severe the higher the Q. The solution is to update the frequency ω_{mod} at which the signal force is modulated to match real-time cantilever frequency measurements. This leads naturally to signal detection based on frequency shift detection (Albrecht, Grutter, Horne and Rugar, 1991), a powerful alternative to amplitude detection.

4.1.3 Frequency detection

The magnetic resonance force signal can be transduced into a shift in the cantilever resonance frequency by arranging that the signal force be applied *in phase* with the cantilever position (note that the displacement of a harmonic oscillator driven at its resonance frequency lags the driving force by 90°). Using the equation of motion for an SHO

$$m\frac{\partial^2}{\partial t^2}z + \frac{m\omega_c}{Q}\frac{\partial}{\partial t}z + kz = k_1 z \tag{51}$$

where m is the effective mass of the cantilever and the term on the right side is the signal force $F = k_1 z$, manifestly synchronized with cantilever position z. This requires that the cantilever be separately driven (by means of e.g., a piezoelectric actuator) at its resonance frequency at constant amplitude z_{osc} by means of a positive feedback circuit in which the cantilever is the frequency determining element. The frequency shift is given by

$$\frac{\delta\omega}{\omega_c} = \frac{F}{2kz_{\mathrm{osc}}} \tag{52}$$

The magnitude of F is given by the change in signal force over a half cycle of cantilever oscillation; the frequency shift is

4.2 Spin manipulation protocols

There are several methods that can be used to manipulate spin magnetization at the resonance frequency of the micromechanical force sensor. The choice of a preferred spin manipulation protocol will depend on spin system properties such as relaxation time T_1.

4.2.1 Cyclic suppression

The Bloch equation (25) show that M_z is suppressed by the application of a strong resonant ($\omega_{\mathrm{rf}} = \omega_{\mathrm{L}}$) field H_1. Either shifting the frequency off resonance or reducing the amplitude allows M_z to recover (on a timescale T_1). In order to achieve the goal of modulating M_z at ω_c the magnetization must substantially recover during one period of cantilever oscillation. Hence $1/T_1$ must be larger than ω_{mod}.

Cyclic suppression is straightforward to apply and effective (Zhang, Roukes and Hammel, 1996). Its primary disadvantage arises from the potential for spurious feedthrough forces due to the modulation of the rf field at ω_c. This undesired excitation can easily swamp the magnetic resonance signal which is occurring at the same modulation frequency.

4.2.2 Anharmonic modulation

A solution to this problem (Bruland, Krzystek, Garbini and Sidles, 1995) lies in simultaneous anharmonic modulation of two experimental parameters such as rf field strength and applied magnetic field H_0:

$$H_0(t) = H_0 + H_0^{\mathrm{mod}}\cos(\omega_z t) \tag{53}$$

$$H_1(t) = H_1^0 + H_1^{\mathrm{mod}}\cos(\omega_1 t) \tag{54}$$

with modulation frequencies satisfying $|\omega_z - \omega_1| = \omega_c$. The intrinsic nonlinearity of magnetic resonance leads to a term in the spin magnetization oscillating at ω_c, whereas spurious excitations occur at frequencies far from ω_c and therefore have negligible influence.

4.2.3 Adiabatic inversion

For systems with long spin relaxation times $1/T_1 \ll \omega_{\mathrm{mod}}$ a method based on coherent, periodic rotation of the spin orientation is preferable. This approach is based on the fact that orientation of the magnetization will follow that of $\mathbf{H}_{\mathrm{eff}}$ if $\mathbf{H}_{\mathrm{eff}}$ is rotated sufficiently slowly, that is if the rotation is adiabatic. This amounts to requiring that the magnetization precess many times about $\mathbf{H}_{\mathrm{eff}}$ in the time required to significantly rotate $\mathbf{H}_{\mathrm{eff}}$ itself. $\mathbf{H}_{\mathrm{eff}}$ can be periodically rotated by modulating either the magnitude of external magnetic field H_0 or by frequency modulation (FM) of H_1 (see Figure 1). Initially a spin ensemble is prepared with a thermal equilibrium magnetization $\mathbf{M}_z$ parallel to $\mathbf{H}_0$ and with $\Delta\omega$ sufficiently large that $\mathbf{H}_{\mathrm{eff}}$ is essentially parallel to $\mathbf{H}_0$. The magnetization is inverted by rotating of $\mathbf{H}_{\mathrm{eff}}$ through 180°, that is, $\Delta\omega$ is swept from a large positive value through zero (resonance) to a large negative value. Adiabaticity is determined by the rate of rotation of $\mathbf{H}_{\mathrm{eff}}$ compared to the magnitude of γH_{eff}; which passes through a minimum on resonance where its magnitude is γH_1. The values of $H_1 \sim 1\text{–}10\,\mathrm{G}$ achievable in MRFM set a limit on

the allowed modulation rate $\omega_{\rm mod}$. For inversion by FM the adiabatic condition requires

$$\omega_{\rm mod} \ll \frac{\gamma^2 H_1^2}{\Delta\omega} \tag{55}$$

4.2.4 MRFM excitation by adiabatic reversals

Examination of equation (15) in Section 2.1.4 reveals two ways to modulate the $\hat{z}$-component of $\mathbf{H}_{\rm eff}$: modulation of $\omega_{\rm rf}$ or modulation of $H^{\rm tot}$. We first consider FM to cyclically reverse $\mathbf{H}_{\rm eff}$:

$$\omega_{\rm rf} = \Omega_{\rm FM}\cos(\omega_{\rm mod} t) \tag{56}$$

In order to generate a frequency shift signal the cantilever is driven into oscillation at its natural resonance frequency ω_c with oscillation amplitude $z_{\rm osc}$, and we set $\omega_{\rm mod} = \omega_c$ and phase lock the reversals to the cantilever position (see Section 4.1.3).

Starting with the magnetization parallel to $\mathbf{H}_0$, $\omega_{\rm rf}$ is set to be far below $\omega_{\rm L}$ for the spins of interest (remember that due to the tip field gradient $\omega_{\rm L}$ varies with position). At the moment the cantilever is at an extremum of its oscillation we begin FM centered on $\omega_{\rm L}$ thus generating adiabatic reversals of the magnetization that will shift the cantilever resonant frequency ω_c. This frequency shift is continuously monitored as it decays with time (Figure 7).

The spins will follow $\mathbf{H}_{\rm eff}$ only if it is rotated sufficiently slowly that the adiabatic condition is satisfied, that is, only if spins precess about $\mathbf{H}_{\rm eff}$ much faster than its orientation rotates. The most demanding moment is at resonance when $|H_{\rm eff}|$ is minimum and equal to H_1; typically $\sim$1–10 G in the microwave regime. Hence, the magnitude of H_1 sets the limit on the modulation rate $\omega_{\rm mod}$ achievable with this method. If $\mathbf{H}_{\rm eff}$ is inverted by rf FM the adiabatic condition is

$$\omega_{\rm mod} \ll \frac{\gamma^2 H_1^2}{\Omega_{\rm FM}} \tag{57}$$

The lifetime τ_m of the signal generated by cyclic adiabatic inversion cannot exceed the spin relaxation time in the rotating frame $T_{1\rho}$. In practice it is also limited by unavoidable violations of adiabatic condition due to insufficient applied rf field strength H_1.

The sign of the frequency shift can be reversed selecting an opposite sign of the signal force relative to the cantilever position, that is, by reversing the cantilever extremum at which FM is commenced. This allows the sign of the signal to be reversed with minimal change to the spurious background providing a means to subtract off this background.

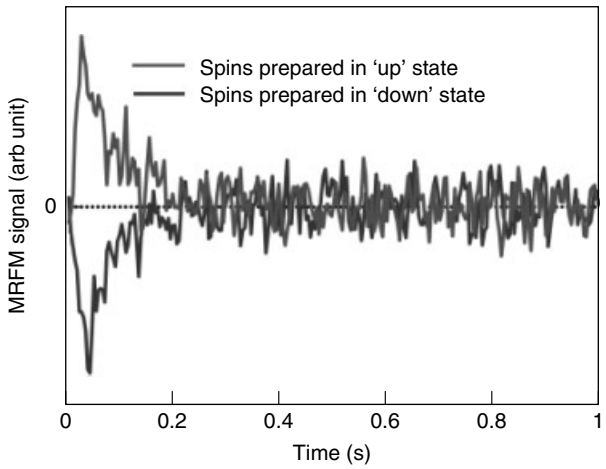

Figure 7. ESR signal at $T = 4$ K from E'-centers in silica detected using OSCAR. The sign of the signal is reversed by preparing the spin system in an inverted state. (Provided by P. Banerjee.)

4.2.5 Oscillating cantilever-driven adiabatic reversals

The technique dubbed oscillating cantilever-driven adiabatic reversals (OSCAR) (Stipe *et al.*, 2001c) was pioneered explicitly for situations where few spins are detected and hence very large gradients are used. OSCAR relies on field modulation in equation (15) to rotate $\mathbf{H}_{\rm eff}$, but uses a clever trick: rather than modulate H_0 advantage is taken of the large field gradient generated by the tip. As the cantilever oscillates this large gradient means that $H_{\rm tip}$ experienced by the spins of interest will be modulated:

$$\delta H_z^{\rm tot} = \delta H_z^{\rm tip} = z_{\rm osc}\frac{{\rm d}H^{\rm tip}}{{\rm d}z} \tag{58}$$

OSCAR naturally inverts the effective field $H_{\rm eff}$ and hence the magnetization with a phase appropriate for frequency shift detection: because the modulation of the field is due to cantilever motion the oscillations are perfectly synchronous with the position of the cantilever (see Figure 1). Consequently, as long as the adiabatic condition (equation (57)) is satisfied the force on the cantilever will be explicitly phase-locked to the position of the cantilever and so the force will shift the resonance frequency of the cantilever.

The OSCAR protocol also begins with the magnetization polarized along $\mathbf{H}_0$. The rf field with its frequency $\omega_{\rm rf}$ well below $\gamma H_{\rm tot}$ is turned on when the cantilever is at an extremum so the effective field $\mathbf{H}_{\rm eff}$ is nearly aligned with $\mathbf{H}_0$. The tip motion will modulate the field causing adiabatic reversals that shift ω_c.

The sign of the frequency shift depends on the phase of the cantilever oscillations relative to the magnetization reversals again providing a means to subtract off spurious backgrounds. This relative phase can be changed, for example, by

preparing spins in a state aligned in the direction opposite to $\mathbf{H}_0$ by means, for example, of an rf π pulse such as is shown in Figure 7. This enables detection of the spin polarization state using MRFM.

We return to the requirement OSCAR places on the field gradient. Successful adiabatic reversal requires $\Delta H_{\mathrm{tot}} \gg H_1$, and since $\Delta H_{\mathrm{tot}} = z_{\mathrm{osc}} \mathrm{d}H^{\mathrm{tip}}/\mathrm{d}z$ we need

$$\frac{\mathrm{d}H^{\mathrm{tip}}}{\mathrm{d}z} \gg \frac{H_1}{z_{\mathrm{osc}}} \tag{59}$$

It is unproductive to make z_{osc} much larger than 100 nm because this reduces the frequency shift (see equation (52)), so for $H_1 \sim 1\text{–}10\,\mathrm{G}$, gradients of order of $0.1\text{–}1\,\mathrm{G\,nm^{-1}}$ are needed.

4.3 Probe–sample interactions

The MRFM probe–sample interaction is given by equation (45). Though this expression is convenient it fails to convey many salient features of the general case. Let us consider a probe magnet creating a spatially nonuniform magnetic field $\mathbf{H}^{\mathrm{tip}}(\mathbf{r})$, where $\mathbf{r}$ is the spatial coordinate, interacting with a time dependent spin magnetization of the sample $\mathbf{m}(\mathbf{r}, t) = \mathbf{m}_0(\mathbf{r}) + \delta\mathbf{m}(\mathbf{r}, t)$ with the time dependent component originating from rf manipulation of spins in the sample. In this case, the time dependent component of the total force between the MRFM probe and the sample will be

$$\mathbf{F}(t) = \int_V (\delta\mathbf{m}(\mathbf{r}, t) \cdot \nabla)\, \mathbf{B}^{\mathrm{tip}}(\mathbf{r})\, \mathrm{d}\mathbf{r} \tag{60}$$

where the integration done over the entire sample volume. The static component of the interaction with $\mathbf{m}_0(\mathbf{r})$ will not be detected by the resonant detection scheme employed in MRFM. To understand MRFM probe–sample interaction, we must analyze the spatial and time dependence of $\delta\mathbf{m}(\mathbf{r}, t)$ and the spatial variation of the gradient of the magnetic field $\mathbf{H}(\mathbf{r})$ of the micromagnetic tip.

4.3.1 Sensitive slice evolution

The spatial variation of $\delta\mathbf{m}(\mathbf{r}, t)$ will depend on the method used for spin manipulation. As an illustrative example we consider the case of cyclic suppression (Section 4.2.1) by means of a 100% amplitude modulation of the intensity of the rf field. The frequency of the rf radiation is ω_{rf}. For simplicity, we assume that the sample is placed in the external magnetic field $\mathbf{H}_0 \parallel \hat{z}$ such that $|\mathbf{H}_0| \gg |\mathbf{H}^{\mathrm{tip}}(\mathbf{r})|$. The thermal spin polarization in this case is $\mathbf{m}_0 = m_0\hat{z}$. The probe magnet is a small magnetic sphere magnetized in the $\hat{z}$ direction. The (spatially dependent) response of the magnetization to the applied rf field is given by equation (25); we find

$$\delta m_z(\mathbf{r}) = \frac{m_0\gamma^2 H_1^2 T_1 T_2}{1 + [T_2(\gamma\,|\mathbf{H}_0 + \mathbf{H}^{\mathrm{tip}}(\mathbf{r})| - \omega_{\mathrm{rf}})]^2 + \gamma^2 H_1^2 T_1 T_2} \tag{61}$$

This equation shows that the applied rf radiation will have the greatest effect on the spins in the spatial volume known as the *sensitive slice* where the following condition is satisfied:

$$|\gamma\,|\mathbf{H}_0 + \mathbf{H}^{\mathrm{tip}}(\mathbf{r})| - \omega_{\mathrm{rf}})| \leq \frac{\delta\omega}{2} \tag{62}$$

Here $\delta\omega = T_2^{-1}$ is the linewidth of the magnetic resonance signal (see equation (25)). The shape of the sensitive slice, a bowl centered on the probe magnet, is defined by both $\mathbf{H}_0$ and $\mathbf{H}^{\mathrm{tip}}(\mathbf{r})$; this shape is shown in Figure 8 for various values of H_0. The radius of the bowl increases with increasing $|\mathbf{H}_0|$ until it transforms into a doughnut-like shape when $|\mathbf{H}_0| > \omega_{\mathrm{rf}}/\gamma$.

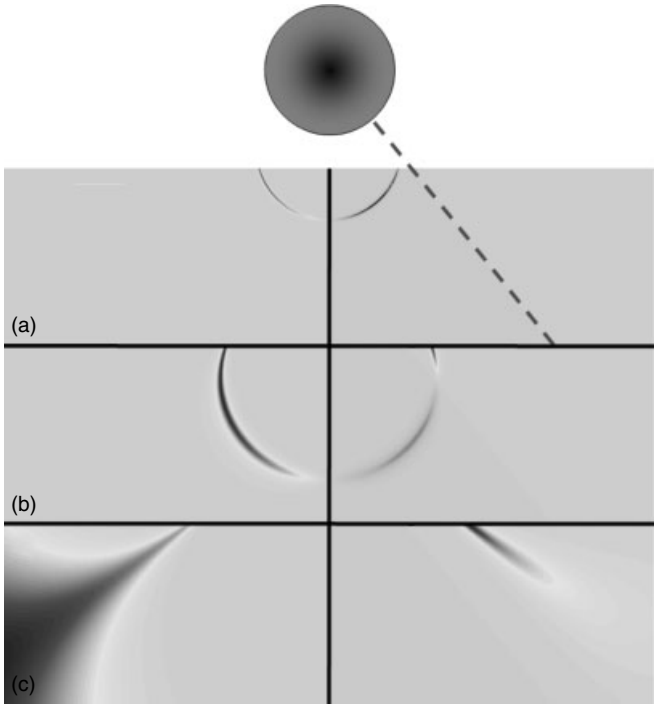

Figure 8. Evolution of the sensitive slice (left panel) and the force slice (right panel) with applied field H_0 increasing from (a) to (c), with (c) corresponding to $H_0 = \omega_{\mathrm{rf}}/\gamma$. The probe magnet of diameter a (shown as the black circle above the sample) and the magnet-sample separation are presented to scale, with the sample width being $5\,a$. The dashed line marks the line of the zero gradient $\mathrm{d}H_z/\mathrm{d}z$. (A color version of this figure is presented in Suter, Pelekhov, Roukes and Hammel, 2002.) (Reprinted with permission A Suter *et al*., copyright 2002, Elsevier.)

4.3.2 Evolution of the force

The magnetization couples to the cantilever through the $\hat{z}$ component of the force $-(\mathbf{m}\cdot\nabla)\mathbf{B}(\mathbf{r})$, hence for the geometry shown in Figure 6 the component of primary interest is $\mathrm{d}H_z/\mathrm{d}z$. The dipolar nature of the probe field means the sign $\mathrm{d}H_z/\mathrm{d}z$ reverses for magnetization off to the side of the tip (see Figure 8), therefore different parts of the sample contribute forces of different sign and, under certain conditions, can cancel one another. Figure 8 shows the evolution of the 'force slice' which is essentially the 'sensitive slice' convolved with the position dependence of the tip gradient. Spins located along the lines of zero gradient do not contribute to the interaction.

4.3.3 Leading edge signal

The spectrum, that is, the evolution of the signal force with field H_0, can be simulated by integrating the force over the entire sample for a series of applied fields. It is typical that the signal changes sign as the shape of the sensitive slice evolves with H_0 (Suter, Pelekhov, Roukes and Hammel, 2002). An important feature of the spectrum is its 'leading edge', that is, the minimum field H_0 at which the signal appears; this occurs as the sensitive slice just enters the surface of the sample. The field offset of this feature from $\omega_{\mathrm{rf}}/\gamma$ measures the strength of the field due to the probe magnet for a particular tip-sample separation.

Measuring the tip field as a function of separation is useful for mapping the spatial variation of tip field with nanometer scale resolution. From this the gradient of the tip field can be accurately obtained. Precise characterization of MRFM probe magnets is essential for correct interpretation of MRFM data.

5 APPLICATIONS

MRFM is a powerful and inventive approach to imaging and characterization of a broad variety of materials. As in the case of conventional magnetic resonance, MRFM is based on direct coupling of the detector to the dipole moment of the target spin. As we have seen in the preceding text because this interaction is quite weak this entails great care in the detection of the signal and has implications for quality and bandwidth of the signal detected. On the other hand, this allows the approach to be applicable to the detection of any spin or spin ensemble that can be brought into the proximity of the micromagnetic probe tip. This excellent breadth of applicability and flexibility distinguishes it from the array of powerful spin sensitive detection techniques currently in use and development.

The true power of MRFM will be determined by the impact of its application to problems studying and developing electronic, magnetic, and structural materials as well as to the biomedical community with extensive need for structural and functional characterization and visualization of biological materials. The rapid pace at which MRFM has improved capabilities such as sensitivity, signal bandwidth, and the rapidly expanding range of materials to which it has been successfully applied suggest a robust technique with the broad flexibility necessary to adapt to the diversity of experimental conditions that will be encountered in performing compelling studies of currently interesting materials.

MRFM offers the excellent sensitivity required to achieve very high spatial resolution. Just as important, this excellent sensitivity comes with a noninvasive probe that will benefit fields from nano-electronics to biomolecular imaging. As electronic elements become smaller, they become sensitive to even individual impurities and dopants; hence three-dimensional atomic scale characterization becomes crucial. Perhaps most notably, the field of spin-based quantum computation will require single spin detection technology both for quantum state readout and for device characterization; single spin MRFM promises to aid in this challenging undertaking.

5.1 Ferromagnetic resonance

There are two motivations for performing FMR experiments using the MRFM. First is the tremendous promise of microscopic FMR experiments for elucidating the nature of scientifically and technologically important magnetic materials such as layered magnetic systems exploiting spin dependent electron transport phenomena. It is important to understand how the performance of such devices is influenced by microscopic spatial variations in properties like interface quality, exchange coupling, and magnetic anisotropy. Conventional FMR has proved to be a powerful technique in evaluating the average values of these properties within the sample.

With the addition of the microscopic imaging capability of MRFM, FMR/MRFM could become one of the primary characterization techniques for such devices (see Wigen, Roukes and Hammel, 2006) for a review of FMR microscopy. Furthermore, unlike conventional inductive detection force detection of magnetic resonance is uniquely sensitive to M_z, the longitudinal component of the magnetization. In the subsequent text, we outline some experiments that exploit these strengths and demonstrate the potential MRFM holds for studies of ferromagnetic materials and devices.

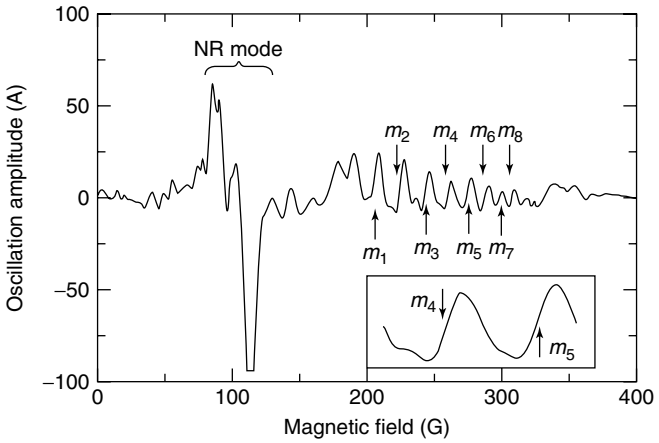

Figure 9. An experimental FMR/MRFM spectrum (cantilever oscillation amplitude as a function of applied field in Gauss) of a single crystal YIG film (Reprinted with permission Z Zhang *et al*., copyright 1996, American Institute of Physics.) which shows the nonresonance (NR) mode and a family of magnetostatic modes (labeled m_1, m_2, ...). The locations of the magnetostatic modes are indicated by arrows in the inset. The resonance was excited by a 2 G, 825 MHz magnetic field; the rf field was 100% amplitude modulated at 41.27 kHz. The bias field was ramped at $1.5\,\mathrm{G\,s^{-1}}$ and modulated at a frequency of 36.01 kHz and with a modulation amplitude of 4 G.

5.1.1 MRFM detection of FMR

The first MRFM detection of FMR (see Figure 9) was demonstrated on a film sample of yttrium iron garnet (YIG) by Zhang, Hammel and Wigen (1996). The sample was an approximately rectangular parallelepiped $20 \times 40 \times 3\,\mu\mathrm{m}^3$ YIG chip that was mounted on the cantilever; the gradient magnet was stationary. The signal was sufficiently large that the experiments were performed in ambient air to reduce Q and the cantilever's oscillatory response. The signal was generated by anharmonic modulation (Bruland, Krzystek, Garbini and Sidles, 1995). The applied magnetic field ranged from 150 to 400 Oe, so the sample was not entirely saturated. As a consequence strong spurious coupling was observed at lower fields where the field was just sufficient to saturate the center of the sample, so modulation of the field significantly altered M_z.

At higher fields, a family of resonance modes, the magnetostatic modes first calculated by Damon and Eshbach (DE) (1961) were observed. The application of DE theory was complicated by the small size and irregular shape of the sample and by the fact that the sample is not fully saturated at resonance. Nonetheless, the results agreed qualitatively with estimates based on DE theory in a rectangularly-shaped, saturated YIG medium. The tip field strength was insufficient to enable local imaging, so the resonance modes observed arose from the resonance behavior of the entire sample.

Wago, Botkin, Yannoni and Rugar (1998) performed FMR on a similar sample, but with gradients as large as $10\,\mathrm{G\,\mu m^{-1}}$ and found similar behavior, namely, that the detected modes were collective modes of the entire sample defined by sample dimensions. Images consistent with this conclusion were observed.

5.1.2 Damping in ferromagnets

Klein and coworkers have performed experiments in which they used MRFM to perform FMR experiments on a 160 μm diameter YIG disk (Klein, Charbois, Naletov and Fermon, 2003; de Loubens, Naletov and Klein, 2005). They exploited both the fact that force detection is sensitive to the longitudinal component of the magnetization rather than the transverse component as in inductive detection and the high sensitivity of MRFM to allow measurements not possible by conventional means. Their measurements were performed on the entire YIG disk with the tip far removed. This work has provided quantitative results that provided unique insights into fundamental dynamic behaviors in ferromagnets.

MRFM detection of FMR differs from conventional approaches in that M_z is directly measured in contrast to measurement of the absorption of microwave power as in conventional FMR detection. They compared power absorbed (proportional to the square of the transverse magnetization M_t^2) to M_z to identify various contributions to the observed FMR linewidth. The enhanced sensitivity provided MRFM detection also allowed detection of the longitudinal moment across a broad range of microwave frequencies even far from the resonance frequency of the microwave resonator.

Their MRFM measurement of the FMR linewidth as a function of frequency from 5 to almost 14 GHz revealed a linear response, that a frequency dependent component and a frequency independent component. The frequency dependent component that is associated with Gilbert damping because of the proportionality to $\partial M/\partial t$, while frequency independent component can have various origins including inhomogeneous broadening and impurity scattering of magnons. The frequency dependence revealed a peak in the linewidth at the resonant frequency of the microwave resonator that was attributed to loading of the resonator by the sample so as to reduce the intensity of H_1 near the Larmor frequency.

While providing insight the homogeneous and inhomogeneous contributions to the linewidth cannot be distinguished on the basis of the frequency dependence alone. It is known that by measuring the dependence of the FMR signal amplitude on the frequency at which the microwave excitation frequency is modulated the relaxation times associated with relaxation via magnetostatic and exchange modes can be

extracted. MRFM detection of the longitudinal magnetization as a function of modulation frequency was used for this measurement in addition to traditional FMR techniques to measure the dependence of the transverse magnetization on the same quantity. For MRFM detection the signal must be generated at ω_c (see Section 4); in order to allow modulation at a broad range of frequencies, Klein *et al*. employed anharmonic modulation (Bruland, Krzystek, Garbini and Sidles, 1995) involving simultaneous frequency and amplitude modulation (at ω_a) of the microwave excitation such that $\left|\omega_f \pm \omega_a\right| = \omega_c$.

The group took advantage of MRFM's unique ability to directly measure M_z They observed a rapid suppression of M_z as saturation of the resonance is approached. This provides new insight into the spin dynamics occurring at saturation. Spin relaxation arises from the generation of spin waves (Suhl and Phys, 1957; Fletcher, LeCraw and Spencer, 1960), but the transverse magnetization is largely insensitive to short wavelength spin wave modes because their transverse component averages to zero, so only measures the number of fundamental mode spin waves. However each spin wave mode reduces the longitudinal magnetization by $\gamma\hbar$ so the longitudinal magnetization measures the total number of spin waves of all wavelengths. As shown in Figure 10, at saturation $1/T_1$ decreases rapidly as the generation of fundamental mode spin waves saturates. Instead there is a rapid increase in the generation of short length spin waves that cannot be detected in conventional transverse linewidth measurements.

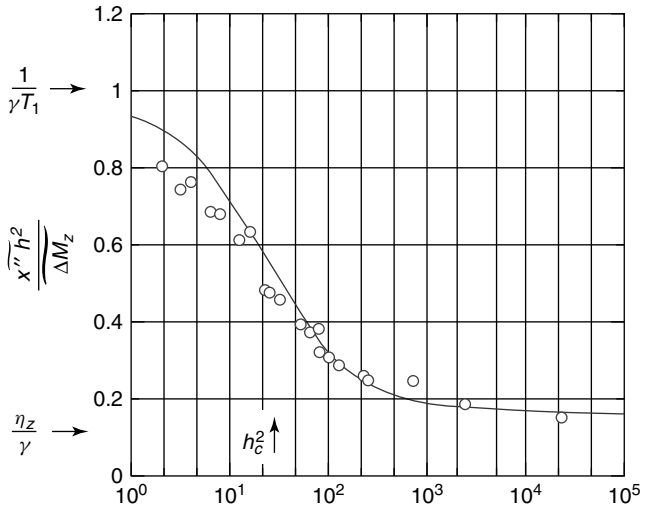

Figure 10. A plot of the ratio of the transverse component of the magnetization relative to the longitudinal component versus microwave power. (Reprinted with permission de Loubens *et al*., copyright 2005, American Physical Society.) This ratio is equal to $1/\gamma T_1$. By comparing conventional and MRFM detected linewidth data, the authors showed the rapid decrease of $1/T_1$ at saturation.

5.1.3 FMR imaging

Mewes *et al*. have demonstrated the ability of MRFM to observe spin dynamics of ferromagnets in micron-scale ferromagnetic structures (Mewes *et al*., 2006). The experiments were performed on an array of permalloy disks 50 nm thick and 1.5 μm in diameter. Experiments were performed both with the tip far from the dots and very close. When distant the tip field was very small and magnetostatic modes in good agreement with theoretical expressions (Kalinikos, 1980) were observed. The MRFM tip used was characterized by means of ESR experiments on DPPH (1,1-Diphenyl-2-picrylhydrazyl) to determine the dependence of the tip field on tip-sample separation.

The sample experiences tip fields in excess of 400 Oe when the tip approaches closely. The external magnetic field was tuned to the spectral feature associated with the fundamental magnetostatic mode and the tip was scanned over the sample (Figure 11). The resolution of the image is much better than that achievable using the same tip (tip width ~1 μm) for MFM of the dots. In fact the spatial resolution is roughly consistent with the ratio of the linewidth of the mode selected for imaging (~40 Oe) and the field gradient (~300 G μm^{-1}); the same ratio that sets spatial resolution in MRI of paramagnetic materials. Thus MRFM allows studies of static and dynamic spin properties in patterned magnets with resolution not set by the tip dimensions as in MFM. However the detailed mechanism of imaging is not understood and the question of spatial resolution achievable in extended ferromagnets remains an area of active study (Mewes *et al*., 2006; Midzor *et al*., 2000; Urban *et al*., 2006).

5.2 Electron spin resonance

Mechanical detection of magnetic resonance was first demonstrated using ESR (Rugar, Yannoni and Sidles, 1992) using an organic molecule DPPH with an unpaired spin that has a rapid (and temperature independent) spin relaxation rate ($T_1 \approx T_2 \approx 60$ ns) and a high spin density (2×10^{21} cm^{-3}). Because $\omega_c \ll 1/T_1$ cyclic suppression must be used to modulate M_z (see Section 4.2.1).

The push to improve detection sensitivity has relied on samples with very long spin relaxation times ($\gg \omega_c^{-1}$) to enable long data collection times and therefore reduced noise bandwidths. In this case, modulation of M_z is accomplished by means of cyclic adiabatic inversion (Section 4.2.3).

That effort produced the milestone of MRFM detection of a single electron spin by (Rugar, Budakian, Mamin and Chui, 2004). This is a signal achievement that dramatically alters the horizons for high-resolution imaging and experimentation on nanoscale systems. It confirms the extraordinary sensitivity of MRFM and underlines the breadth and flexibility of

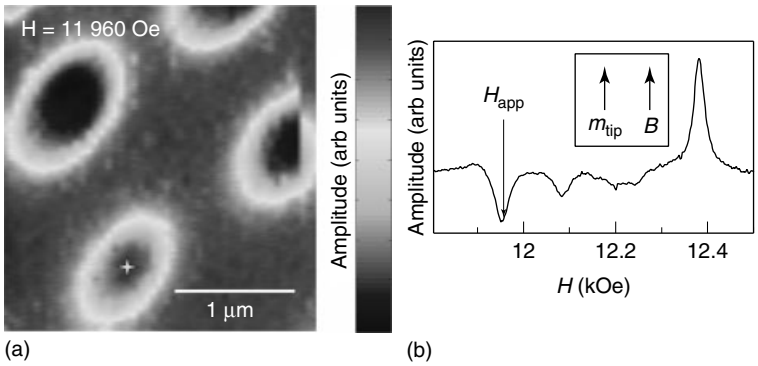

Figure 11. Images obtained at a tip-sample separation of 150 nm and a microwave frequency of $f_{mw} = 7.7\,\text{GHz}$ 60% amplitude modulated at the cantilever frequency are shown. (b) shows the MRFM spectrum obtained with the tip located over the center of the permalloy dot (indicated by the star). (a) shows the cantilever response obtained in lateral scans over an area $2.5 \times 2.5\,\mu\text{m}^2$ at a field $H = 11\,960\,\text{Oe}$. The external magnetic field was aligned parallel to the moment of the tip.

the method. The experiment was done on a silica sample containing a low density ($\sim 10^{14}\,\text{cm}^{-3}$) of electronic spins known as E′ centers that are created by γ-irradiation of the silica. The low spin density ensured that an isolated spin could be found for detection by the MRFM micromagnetic tip.

5.2.1 Single electron spin detection

The ultrahigh sensitivity regime involves several extreme parameter values that lead to new phenomena:

- Very high sensitivity enables detection of ensembles sufficiently small that the thermal fluctuations of the net spin polarization dominate over the thermal equilibrium polarization.
- The large tip field gradients necessary for high sensitivity lead to large temporal variations of the magnetic field as a consequence of cantilever motion; these can be beneficial or detrimental.

Statistical spin polarization

For sufficiently small ensembles thermal fluctuations of the net spin polarization can be an important effect: the net spin polarization is proportional to

$$\Delta N = N_\uparrow - N_\downarrow = \sqrt{N} \tag{63}$$

This 'statistical polarization' becomes comparable to the thermal equilibrium Boltzmann polarization at $T = 4\,\text{K}$ and $H = 1\,\text{kOe}$ for samples containing of order 10^4 spins. One can then achieve larger signals and can collect data continuously avoiding the need to wait for the spin polarization to recover to thermal equilibrium by means of spin-lattice relaxation before the next measurement.

On the other hand the average polarization and hence average signal is zero, and so the spin magnetic resonance response is manifested only in the variance of the force signal (Budakian, Mamin, Chui and Rugar, 2005). Instead of a definite frequency shift the cantilever undergoes random frequency fluctuations (see Figure 12) of magnitude

$$\delta f_c = \pm f_c \frac{2\mu_B \sqrt{N} \nabla H_z}{\pi k z_{osc}} \tag{64}$$

With field gradient $\nabla H_z \approx 2\,\text{G nm}^{-1}$ and a very small cantilever spring constant $k \approx 0.1\,\text{mN m}^{-1}$ the frequency shift per electronic spin is $\sim$3–5 mHz assuming $z_{osc} = 16\,\text{nm}$.

Interrupted OSCAR

This challenge led to the development of a variant of the OSCAR (Rugar, Budakian, Mamin and Chui, 2003) technique (Section 4.2.5) in which the motion of the micromagnetic tip mounted on the driven cantilever cyclically reverses the orientation of H_{eff} and hence the spin orientation. Dubbed iOSCAR (Mamin, Budakian, Chui and Rugar, 2003) it employs an interruption of the rf field for half a cantilever period that allows the cantilever to move from one extremum to another without rotating H_{eff}. The spin force remains proportional to the cantilever position, but the phase of the oscillatory force exerted on the cantilever relative to its position is reversed thus changing the sign of the resulting frequency shift (see Figure 13). This modulates the OSCAR signal and imprints the signal with a time signature that allows it to be identified at nonzero offset frequency from $f_c = \omega_c/2\pi$.

If the rf power is interrupted at a frequency $f_{int} = 86\,\text{Hz}$ the cantilever frequency is modulated at $f_{sig} = f_{int}/2 = 43\,\text{Hz}$. The frequency shift associated with the magnetic

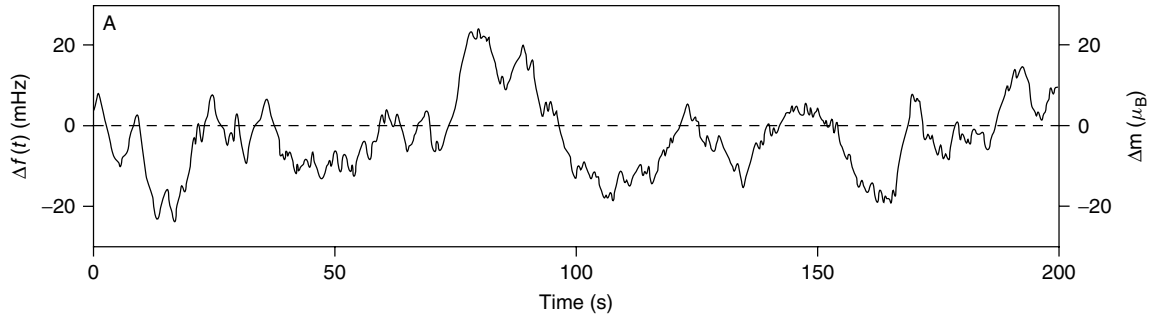

Figure 12. Trace showing a time record of the statistical fluctuations. (Reprinted with permission Budakian *et al*., copyright 2005, AAAS.) The frequency shift recorded in a 83-mHz bandwidth is converted to equivalent number of spins (right-hand axis) by dividing Δf by the average frequency shift per spin ($\overline{|\delta f|} = 0.8$ mHz/spin).

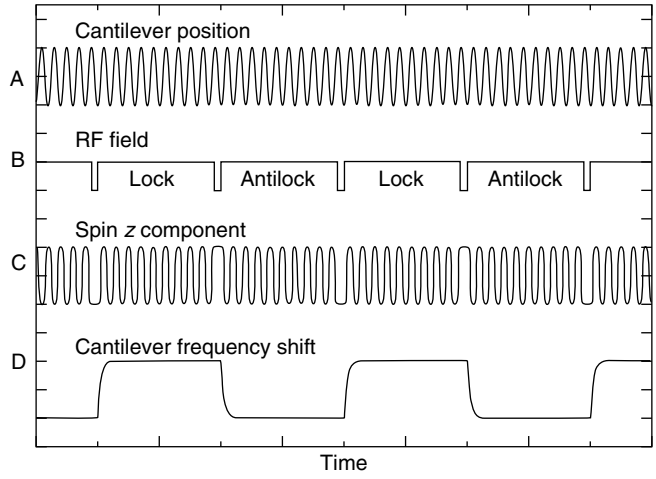

Figure 13. Timing diagram for the interrupted OSCAR protocol. (Reprinted with permission Mami *et al*., copyright 2003, American Physical Society.) The cantilever is oscillated continuously at its resonance frequency, and the microwave field (curve B) is normally on, but is periodically interrupted for one-half cantilever cycle. The z component of the magnetization (C) oscillates in response to the cantilever motion due to adiabatic rapid passage when the microwaves are on, but is left static when they are off. The oscillating magnetization reverses phase with respect to the cantilever for each microwave interruption, giving a cantilever frequency shift (D) that oscillates at one-half the microwave interrupt frequency (F).

resonance alone will manifest itself at this frequency with an intensity

$$\Delta f(t) = \frac{4}{\pi}|\delta f_c| A(t) \tag{65}$$

where $A(t)$ represents the random statistical fluctuations (Rugar, Budakian, Mamin and Chui, 2004).

Signal averaging presents an unusual challenge in this case since the average signal is zero: $\langle A(t)\rangle = 0$, hence $\langle \Delta f(t)\rangle = 0$, and $\langle [A(t)]^2\rangle = 1$. Hence to obtain a signal the square of the frequency shift $[\Delta f(t)]^2$, that is, the signal energy (Rugar, Budakian, Mamin and Chui, 2004) was detected. The phase sensitive lock-in detection can be adjusted such that the signal force appears only in the in-phase variance of the measured signal can be written as $\sigma_I^2 = \sigma_{\text{spin}}^2 + \sigma_{\text{noise}}^2$, where σ_{spin}^2 and σ_{noise}^2 are uncorrelated variances of the spin signal and the noise respectively; the quadrature variance σ_Q^2 will then contain only noise, that is, $\sigma_Q^2 = \sigma_{\text{noise}}^2$. The spin signal is $\sigma_{\text{spin}}^2 = \sigma_I^2 - \sigma_Q^2$ and the signal-to-noise ratio $\text{SNR} = \sigma_{\text{spin}}^2/\sigma_I^2$.

Using this technique the signal from a single electron spin was detected. The low spin density of the sample provides for a 200–500 nm spacing between the spins, whereas while the detected spin sufficiently dilute that the probe can interact only with one spin at a time (see Figure 14). The force variance was $|\delta f_c| = 4.2$ mHz in very good agreement with the expected value. The consistency spatial shift of the signal with change of microwave frequency and the expected value of the force signal variance verified that the signal originates indeed from a magnetic resonance signal.

5.2.2 *Spin relaxation by thermal motion of high gradient tip*

The lifetime of a spin signal during a cyclic inversion measurement is a crucial parameter as short lifetimes spread the signal in frequency space requiring wider bandwidth and hence increased noise. Sensitive experiments require close approach of the magnetic tip to the spin to be detected, but early ESR MRFM experiments showed substantial reduction of the rotating frame electron spin relaxation time τ_m as the tip approached the spin. Rugar *et al*. found that τ_m was reduced from 275 ms to 68 ms as the tip-spin spacing was reduced from 1500 nm to 800 nm (Stipe *et al*., 2001c).

The excess relaxation was found to arise from the magnetic field fluctuations that result when thermal vibrations displace the high gradient tip (Mozyrsky, Martin, Pelekhov and Hammel, 2003). As discussed in Section 2.1.3 the component of

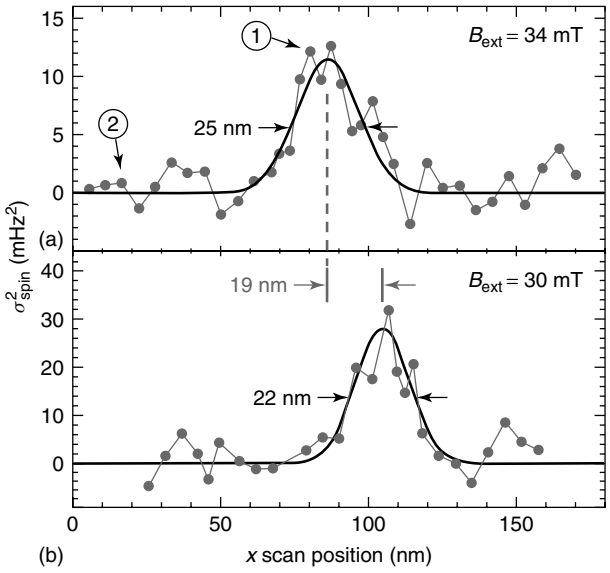

Figure 14. A graph (Reprinted with permission D Rugar *et al*., copyright 2004, Nature Publishing Group.) showing the spin signal as the probe magnet is scanned laterally in the **x** direction across a single electron in a SiO_2 for two values of external field: (a), B_{ext} = 34 mT, and (b), B_{ext} = 30 mT. The smooth curves are Gaussian fits to guide the eye. The 19 nm shift in peak position reflects the movement of the resonant slice induced by the 4 mT change in external field. The difference in absolute peak height is primarily due to different lock-in amplifier detection bandwidths: 0.18 Hz and 0.59 Hz for (a) and (b), respectively.

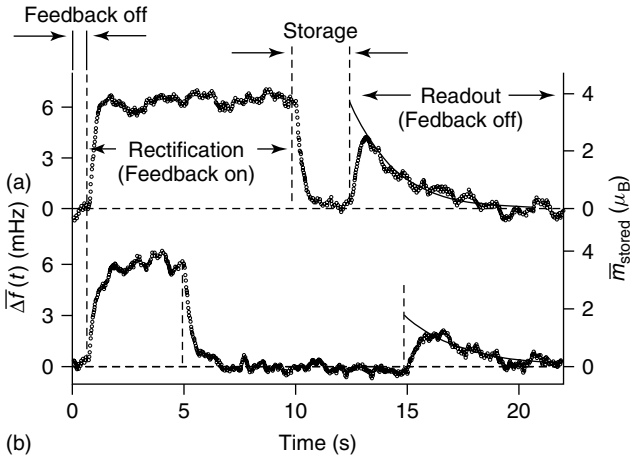

Figure 15. Control of the spin magnetization of few spin ensembles using MRFM (Reprinted with permission Budakian *et al*., copyright 2005, AAAS.) is shown. (a) An average polarization of about 3.7 μ_B was created in an ensemble of $N \approx 70$ spins through active feedback, stored in the laboratory frame for 2.5 seconds, and subsequently read out. (b) Data taken under the same conditions as (a) except that the storage time has been extended to 10 s.

these transverse magnetic field fluctuations at the Larmor frequency ω_L will induce spin relaxation. During the adiabatic inversion the magnetization precesses at frequency $\omega_L(t) = \gamma H_{eff}(t)$; the minimum frequency will be $\omega_L = \gamma H_1$, corresponding to a precession frequency of $\omega_L/2\pi \approx 3$–10 MHz. Though the fundamental cantilever mode is at $\omega_c/2\pi$, typically in the range 1–10 kHz, higher cantilever harmonics can significantly contribute to spin relaxation. It was shown (Mozyrsky, Martin, Pelekhov and Hammel, 2003; Berman, Gorshkov, Rugar and Tsifrinovich, 2003) that the electron spin relaxation rate due to the higher order cantilever modes is

$$\frac{1}{\tau_m} \approx \frac{3.4\mu_B \nabla \mathbf{H}_{probe}}{\hbar} \left(\frac{k_B T}{k\sqrt{z_0^2 - z_1^2}} \right) \left(\frac{\omega_c}{\gamma H_1} \right)^{3/2} \qquad (66)$$

where z_0 is the amplitude of thermal cantilever motion, z_1 is the tip-sample separation, k is the cantilever spring constant and T is temperature. As the probe is brought close to the sample the strength of the probe field gradient $\nabla \mathbf{H}_{probe}$ and hence the induced relaxation rate increases. It is noteworthy that increasing H_1 also reduces excess relaxation.

This problem was conclusively addressed in the single spin experiment (Rugar, Budakian, Mamin and Chui, 2004) where a cantilever designed with an extra mass at its tip to suppress high order vibrational modes effectively eliminated the excess relaxation (Chui *et al*., 2003). H_1 intensity was increased to 7 G through use of a superconducting microwave circuit (Mamin, Budakian and Rugar, 2003). As a result the rotating frame electron spin relaxation τ_m of a single electron was estimated to be 760 ms in the tip field gradient of 2.0 G nm^{-1} ≈250 nm away from the detected spin.

5.2.3 Creating order in spin ensembles

Complementary to high-resolution imaging is the ability MRFM provides to controllably manipulate spin magnetization using spatially localized magnetic resonance. This kind of close control has been nicely demonstrated in experiments that have built on the high sensitivity ESR detection (Budakian, Mamin, Chui and Rugar, 2005).

The first experiment involved hyperpolarizing an electron spin ensemble by capturing an especially large statistical fluctuation (Budakian, Mamin, Chui and Rugar, 2005). In this experiment, the cantilever signal frequency shift $\Delta f(t)$ was continuously monitored, and when the frequency shift exceeded a certain threshold value the rf field was turned off (see Figure 15). Without an rf field cantilever electron spins remain oriented along $\hat{\mathbf{z}}$ and are unaffected by cantilever oscillation so their polarization is effectively preserve for times of order T_1 (measured to be ≈30 s). Spin polarization exceeding anything achievable by thermal polarization could be generated and used in other experiments.

The second experiment building on this idea controlled the spin dynamics of the through real-time feedback. Whenever the frequency shift fell below a certain value a π-inversion was applied. This prevented the system from evolving beyond the predefined polarization. By this means the spin system was locked into a relatively well defined polarization state.

5.3 Nuclear magnetic resonance

NMR is a powerful tool for material studies. Nuclear spins are prevalent in most materials and chemical specificity is achieved since each nuclear spin has a unique gyromagnetic ratio. This has made high sensitivity MRFM detection of NMR a key goal. Excellent progress has been made since the first detection of NMR by means of MRFM in 1993 (Rugar *et al*., 1994).

5.3.1 Detection and manipulation of statistical polarization

State-of-the-art sensitivity has been demonstrated in an experiment (Mamin, Budakian, Chui and Rugar, 2005) that detected the statistical spin polarization of nuclear spins. Nuclear moments are $\sim 10^3$ times smaller than electronic moments, so this approach requires very high sensitivity. The ability to achieve substantial polarization without waiting T_1 is even more advantageous than for electron spin detection because nuclear T_1s can exceed hours at low temperatures.

Three nuclear spin systems were used in this study: ^{19}F nuclei in CaF_2, and ^{1}H spins in the polymer polymethylmethacrylate (PMMA) and collagen. The CaF_2 experiment demonstrated spin sensitivity of $\approx$2000 nuclear spins with a 2.5 h averaging time.

Techniques based on short rf pulses inserted into the interrupted OSCAR protocol described in Section 5.2.1 were developed for spin nutation and transverse spin relaxation measurements using statistically polarized spin ensembles. During the nutation experiment, an rf pulse of length t_p was inserted during the cantilever cycle when the nuclear spins are precisely on resonance causing them to precess about the $\mathbf{H}_{\text{eff}}$ which lies in the $\hat{x}$ plane in the rotating frame of reference. As the pulse length, and therefore the angle of spin rotation, is changed the signal oscillates with period $T = 2\pi/\gamma H_1$ as shown in Figure 16.

The inhomogeneous transverse spin relaxation time measurement is similar but is based on sequence of two $\pi/2$ pulses separated by a time τ inserted into the iOSCAR sequence. The first pulse rotates spins into the $\hat{x}$-$\hat{y}$ plane where the spin polarization decays due to transverse spin relaxation in a time $T_2^* = 4\,\mu$s. For τ significantly longer than T_2^*, the final polarization vanishes so the signal will be half of the value observed for short τ.

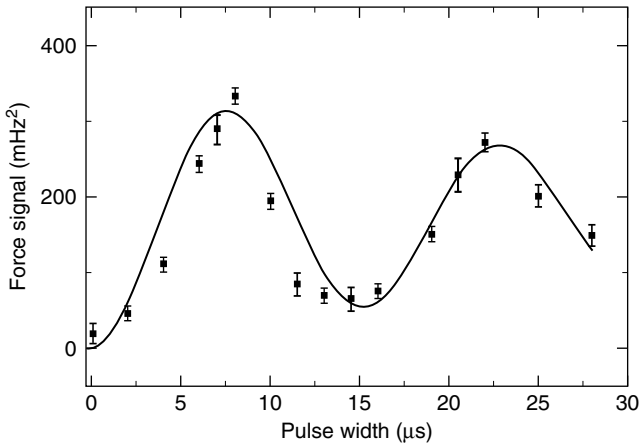

Figure 16. Nutation of the statistical polarization in CaF_2. (Reprinted with permission H J Mamin *et al*., copyright 2005, American Physical Society.) The signal is shown as a function of the pulse width t_p. The spin oscillation period about the effective field indicates an rf field strength $H_1 = 17$ Oe.

This demonstration of standard pulse techniques in combination with ultrasensitive NMR detection reinforces the expectation that MRFM detected NMR will be a powerful tool for microscopic studies of materials.

5.3.2 NMR double resonance in force microscopy

We have seen that MRFM allows NMR detection with the sensitivity much higher than that of the conventional NMR (2000 spins in the IBM experiment, (Mamin, Budakian, Chui and Rugar, 2005) compared to at least 10^{12}–10^{13}). To fully exploit this strength the conventional pulsed NMR techniques must be brought to bear. Important steps in this direction have been demonstrated by (Lin *et al*., 2006). Here we briefly describe their application of solid-state double resonance techniques in an MRFM experiment performed on ^{19}F and ^{31}P nuclei in a KPF_6 crystal.

A useful and commonly used solid-state NMR double resonance technique is Hartmann–Hahn cross polarization (CP) in which polarization transfer from a more easily polarized spin species (e.g., due to a higher gyromagnetic ratio) to a less polarized species provides increased detection sensitivity for the latter. The technique employs irradiation at two rf frequencies (ω_{L}^I and ω_{L}^{II}) with H_1 intensities chosen such that $\gamma^{\text{I}} H_1^{\text{I}} = \gamma^{\text{II}} H_1^{\text{II}}$.

The applicability of these techniques to MRFM detection in the presence of the gradient from a 0.5-mm iron wire has been explored in samples containing $\sim 10^{15}$ spins. Figure 17 shows the growth of the ^{31}P spin polarization as a function of the time τ_{cp} the cross polarization rf field is applied. The

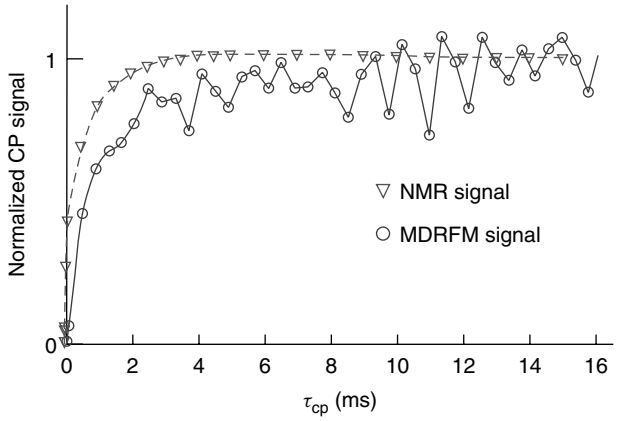

Figure 17. The buildup of the ^{31}P spin polarization as a function of τ_{cp} of the CP pulse sequence was measured using cyclic adiabatic inversion (○). Data acquired in a conventional NMR experiment on the same spin system (▽). (Reprinted with permission Q Lin *et al*., copyright 2006, American Physical Society.)

MRFM data are in good agreement with data acquired in a conventional NMR experiment.

Spin decoupling

Another application of double resonance is to narrow resonance lines in to enhance the resolution of solid-state NMR spectroscopy. A common broadening mechanism in solids results from the interaction between the target spin and neighboring dissimilar spins (heteronuclear coupling). This interaction can be reduced by irradiating at the Larmor frequency of the offending species to average the interaction to zero. During decoupling the target signal is detected at its Larmor frequency.

The Meier group has also demonstrated (Lin *et al*., 2006) narrowing of the ^{31}P line through continuous wave (CW) decoupling applied at the ^{19}F Larmor frequency. The ^{31}P linewidth was measured using a Hahn echo technique in which the echo amplitude is measured using cyclic adiabatic inversion to generate the MRFM signal (Degen *et al*., 2005). The Hahn echo alone will also reduce heteronuclear line broadening but CW decoupling is superior. The linewidth after the echo was 1.4 kHz, this was reduced to 900 Hz by decoupling.

The ability to use pulsed techniques to improve spectral resolution in MRFM is an important advance: when combined with high sensitivity MRFM detection it points toward the potential for local NMR spectroscopy with unprecedented spatial resolution.

5.3.3 1D NMR MRFM imaging of GaAs

The demonstration of NMR/MRFM imaging of Ga in GaAs by D. Smith and colleagues (Thurber, Harrell and Smith, 2003) indicates the promise MRFM holds for studies of microelectronic devices composed of important electronic semiconductors. For multicomponent devices the unique ability of MRFM to observe buried structures is a key strength.

Thurber and Smith *et al*. have obtained 1D NMR/MRFM images of a GaAs sample mounted on the cantilever. Even at $T = 5$ K in a 4 T applied magnetic field the nuclear spin polarization is small, so they optically pumped the electron spin polarization with circularly polarized light to enhance the nuclear polarization. Distinct NMR signals from three nuclear isotopes: (^{71}Ga, ^{69}Ga, and ^{75}As), were detected using cyclic adiabatic inversion. In addition, they obtained high resolution, 1D ^{71}Ga MRFM images from the GaAs sample whose nuclear spin polarization was controllably modified prior to imaging. The optically pumped nuclear magnetization was artificially suppressed by prolonged cyclic adiabatic inversion in two spatial regions separated by a volume of unperturbed magnetization. The MRFM signal was subsequently recorded as the sensitive slice was swept through the sample during the imaging cycle; this revealed the two regions of diminished magnetization at different values of the applied field as shown in Figure 18. The regions can still be resolved as their separation is reduced to 500 nm. The authors estimate their limiting 1D spatial resolution in the experiment to be 170 nm with detection sensitivity of $\sim 4 \times 10^{11}$ ^{71}Ga Hz$^{-1/2}$.

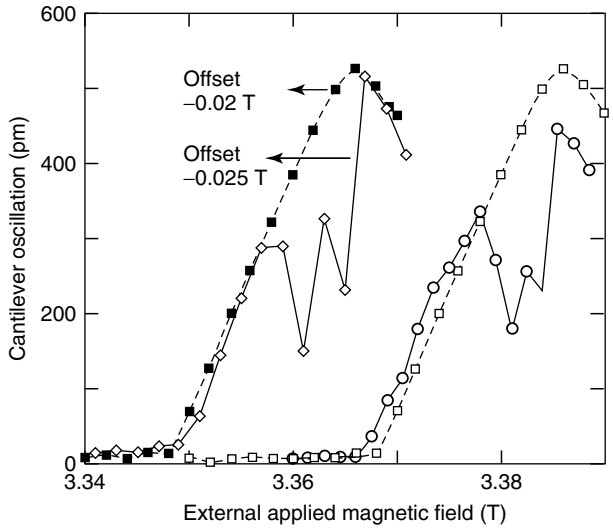

Figure 18. Demonstration of spatially resolved NMR in optically pumped ^{71}Ga. (Reprinted with permission K R Thurber *et al*., copyright 2003, Elsevier.) The spin polarization was suppressed in two closely spaced slices and then imaged for two slice separations: 670 nm (◇) and 500 nm (○). For comparison, spectra obtained from optically pumped sample with no slice saturation are shown (□ and ■). (The difference in offset between the unmodified (■, offset −0.02 T) and the 670 nm (◇, offset −0.025 T) data is believed to be caused by a slight change <1 μm in the separation between the sample and magnet for these data runs done on different days.

6 CONCLUSIONS

We have discussed the methods and techniques of MFRM, an emerging fully three-dimensional high-resolution scanned-probe technique. While focusing on detailed discussions of the experimental approaches used, we have also pointed out several successful applications. The rapid improvement in the capabilities of the technique culminating notably in the detection of individual electronic spins demonstrate that it is a robust and flexible technique. The range of successful applications serve to confirm this and indicate its broad potential.

ACKNOWLEDGMENTS

We thank P. Banerjee and R. Steward for allowing us to use unpublished figures. We also gratefully acknowledge the Department of Energy Office of Basic Energy Sciences, the Army Research Office and the National Science Foundation for their support of the authors' work reported in this article.

REFERENCES

Abragam, A. (1961). *The Principles of Nuclear Magnetism*, Clarendon: Oxford.

Albrecht, T.R., Grutter, P., Horne, D. and Rugar, D. (1991). Frequency Modulation detection using High-Q cantilevers for enhanced force microscopy sensitivity. *Journal of Applied Physics*, **69**, 668.

Albrecht, T.R., Grütter, P., Rugar, D. and Smith, D.P.E. (1992). Low temperature force microscope with all-fiber interferometer. *Ultramicroscopy*, **42–44**, 1638–1646.

Arlett, J.L., Maloney, J.R., Gudlewski, B., *et al*. (2006). Self-sensing micro- and nanocantilevers with attonewton-scale force resolution. *Nano Letters*, **6**(5), 1000–1006.

Barrett, T.A., Miers, C.R., Sommer, H.A., *et al*. (1998). Design and construction of a sensitive nuclear magnetic resonance force microscope. *Journal of Applied Physics*, **83**, 6235.

Berman, G.P., Gorshkov, V.N., Rugar, D. and Tsifrinovich, V.I. (2003). Spin relaxation caused by thermal excitations of high-frequency modes of cantilever vibrations. *Physical Review B*, **68**, 94402.

Bloch, F. (1946). Nuclear induction. *Physical Review*, **70**, 460.

Bruland, K.J., Dougherty, W.M., Garbini, J.L., *et al*. (1998). Force-detected magnetic resonance in a field gradient of 250,000 Tesla per meter. *Applied Physics Letters*, **73**, 3159.

Bruland, K.J., Garbini, J.L., Dougherty, W.M. and Sidles, J.A. (1996). Optimal control of force microscope cantilevers. II. Magnetic coupling implementation. *Journal of Applied Physics*, **80**, 1959.

Bruland, K.J., Garbini, J.L., Dougherty, W.M. and Sidles, J.A. (1998). Optimal control of ultrasoft cantilevers for force microscopy. *Journal of Applied Physics*, **83**, 3972.

Bruland, K.J., Krzystek, J., Garbini, J.L. and Sidles, J.A. (1995). Anharmonic modulation for noise reduction in magnetic resonance force microscopy. *Review of Scientific Instruments*, **66**, 2853.

Budakian, R., Mamin, H.J., Chui, B.W. and Rugar, D. (2005). Creating order from random fluctuations in small spin ensembles. *Science*, **307**, 408.

Callaghan, P.T. (1991). *Principles of Nuclear Magnetic Resonance Microscopy*, Clarendon Press: Oxford.

Chabot, M.D. and Moreland, J. (2003). Micrometer-scale magnetometry of thin Ni80Fe20 films using ultrasensitive microcantilevers. *Journal of Applied Physics*, **93**, 7897.

Chui, B.W., Hishinuma, Y., Budakian, R., *et al*. (2003). *TRANSDUCERS '03. 12th International Conference on Solid-State Sensors, Actuators and Microsystems*, Digest of Technical Papers, IEEE: Piscataway, pp. 1120–1123, Vol. 2.

Ciobanu, L., Seeber, D.A. and Pennington, C.H. (2002). 3D MR microscopy with resolution. 3.7 μm by 3.3 μm. *Journal of Magnetic Resonance*, **158**, 178.

Damon, R. and Eshbach, J. (1961). Magnetostatic modes of a ferromagnet slab. *Journal of Physics and Chemistry of Solids*, **19**, 308.

Degen, C.L., Lin, Q., Hunkeler, A., *et al*. (2005). Microscale localized spectroscopy with a magnetic resonance force microscope. *Physical Review Letters*, **94**, 207601.

Devoret, M.H. and Schoelkopf, R.J. (2000). Amplifying quantum signals with the single-electron transistor. *Nature*, **406**, 1039.

Fletcher, R.C., LeCraw, R.C. and Spencer, E.G. (1960). Electron spin relaxation in ferromagnetic insulators. *Physical Review*, **117**, 955.

Fukushima, E. and Roeder, S.B.W. (1981). *Experimental Pulse NMR a Nuts and Bolts Approach*, Addison-Wesley: Reading.

Giessibl, F.J. (2003). Advances in atomic force microscopy. *Reviews of Modern Physics*, **75**, 949.

Hammel, P.C., Zhang, Z., Midzor, M. (1998). In *Frontiers in Magnetism of Reduced Dimension Systems*, Wigen, P.E. (Ed.), Kluwer Academic Publishers: Dordrecht.

Hammel, P.C., Zhang, Z., Moore, G.J. and Roukes, M.L. (1995). Subsurface imaging with the magnetic-resonance force microscope. *Journal of Low Temperature Physics*, **101**, 59.

Hoen, S.T., Züger, O., Yannoni, C.S., *et al*. (1994). *Solid-State Sensor and Acutator Workshop*, Hilton Head South Carolina, 13–16 June, Vol. 75, p. 6211.

Kalinikos, B.A. (1980). Excitation of propagating spin waves in ferromagnetic films. *IEEE Proceedings*, **127**, (pt.H), 4.

Klein, O., Charbois, V., Naletov, V.V. and Fermon, C. (2003). Measurement of the ferromagnetic relaxation in a micron-size sample. *Physical Review B: Condensed Matter and Materials Physics*, **67**, 220407.

LaHaye, M.D., Buu, O., Camarota, B. and Schwab, K. (2004). Approaching the quantum limit of a nanomechanical resonator. *Science*, **304**, 74.

Lin, Q., Degen, C.L., Tomaselli, M., *et al*. (2006). Magnetic double resonance in force microscopy. *Physical Review Letters*, **96**, 137604.

de Loubens, G., Naletov, V.V. and Klein, O. (2005). Reduction of the spin-wave damping induced by nonlinear effects. *Physical Review B: Condensed Matter and Materials Physics*, **71**, 180411.

Madou, M.J. (2002). *Fundamentals of Microfabrication: the Science of Miniaturization*, *Second Edition*, CRC Press: Boca Raton.

Mamin, H.J., Budakian, R., Chui, B.W. and Rugar, D. (2003). Detection and manipulation of statistical polarization in small spin ensembles. *Physical Review Letters*, **91**, 207604.

Mamin, H.J., Budakian, R., Chui, B.W. and Rugar, D. (2005). Magnetic resonance force microscopy of nuclear spins: Detection and manipulation of statistical polarization. *Physical Review B: Condensed Matter and Materials Physics*, **72**, 024413.

Mamin, H.J., Budakian, R. and Rugar, D. (2003). Superconducting microwave resonator for millikelvin magnetic resonance force microscopy. *Review of Scientific Instruments*, **74**, 2749.

Mertz, J., Marti, O. and Mlynek, J. (1993). Regulation of a microcantilever response by active control. *Applied Physics Letters*, **62**, 2344.

Mewes, T., Kim, J., Pelekhov, D.V., *et al*. (2006). Ferromagnetic resonance force microscopy studies of arrays on micron size permalloy dots. *Physical Review B*, **74**, 144424.

Midzor, M.M., Wigen, P.E., Pelekhov, D.V., *et al*. (2000). Imaging mechanisms of force detected FMR microscopy. *Journal of Applied Physics*, **87**, 6493.

Mozyrsky, D., Martin, I., Pelekhov, D. and Hammel, P.C. (2003). Theory of spin relaxation in magnetic resonance force microscopy. *Applied Physics Letters*, **82**, 1278.

Pelekhov, D.V., Martin, I., Suter, A., *et al*. (2002). Magnetic resonance force microscopy and the solid state quantum computer. *Proceedings of the SPIE - The International Society for Optical Engineering*, **4656**, 1.

Pelekhov, D.V., Selcu, C., Banerjee, P., *et al*. (2005). Light-free magnetic resonance force microscopy for studies of electron spin polarized systems. *Journal of Magnetism and Magnetic Materials*, **286**, 324.

Rugar, D., Budakian, R., Mamin, H.J. and Chui, B.W. (2003). Manipulation and detection of electron spins by magnetic resonance force microscopy authors. *AIP Conference Proceedings*, **696**, 45.

Rugar, D., Budakian, R., Mamin, H.J. and Chui, B.W. (2004). Single spin detection by magnetic resonance force microscopy. *Nature*, **430**, 329.

Rugar, D., Yannoni, C.S. and Sidles, J.A. (1992). Mechanical detection of magnetic resonance. *Nature*, **360**, 563.

Rugar, D., Züger, O., Hoen, S.T., *et al*. (1994). Force detection of nuclear magnetic resonance. *Science*, **264**, 1560.

Sidles, J.A. (1991). Noninductive detection of single-proton magnetic resonance. *Applied Physics Letters*, **58**, 2854.

Sidles, J.A. (1992). Folded stern-gerlach experiment as a means for detecting nuclear magnetic resonance in individual nuclei. *Physical Review Letters*, **68**, 1124.

Sidles, J.A., Garbini, J.L., Bruland, K.J., *et al*. (1995). Magnetic resonance force microscopy. *Reviews of Modern Physics*, **67**, 249.

Slichter, C.P. (1989). *Principles of Magnetic Resonance*, Springer-Verlag: New York.

Stipe, B.C., Mamin, H.J., Stowe, T.D., *et al*. (2001a). Noncontact friction and force fluctuations between closely spaced bodies. *Physical Review Letters*, **87**(9), 096801.

Stipe, B.C., Mamin, H.J., Stowe, T.D., *et al*. (2001b). Noncontact friction and force fluctuations between closely spaced bodies. *Physical Review Letters*, **86**, 2874.

Stipe, B.C., Mamin, H.J., Yannoni, C.S., *et al*. (2001c). Electron spin relaxation near a micron-size ferromagnet *Physical Review Letters*, **87**(27), 277602.

Stowe, T., Yasumura, K., Kenny, T., *et al*. (1997). Attonewton force detection using ultrathin silicon cantilevers. *Applied Physics Letters*, **71**, 288.

Suhl, H. and Phys, J. (1957). The theory of ferromagnetic resonance at high signal powers. *Chemistry of Solids*, **1**, 209.

Suter, A., Pelekhov, D.V., Roukes, M.L. and Hammel, P.C. (2002). Probe-sample coupling in the magnetic resonance force microscope. *Journal of Magnetic Resonance*, **154**, 210.

Thurber, K.R., Harrell, L.E. and Smith, D.D. (2003). 170 nm nuclear magnetic resonance imaging using magnetic resonance force microscopy. *Journal of Magnetic Resonance*, **162**, 336–340.

Urban, R., Putilin, A., Wigen, P., *et al*. (2006). Perturbation of magnetostatic modes observed by ferromagnetic resonance force microscopy. *Physical Review B*, **73**, 212410.

Wago, K., Botkin, D., Yannoni, C.S. and Rugar, D. (1998). Paramagnetic and ferromagnetic resonance imaging with a tip-on-cantilever magnetic resonance force microscope. Microstrip resonators for electron-spin resonance. *Applied Physics Letters*, **72**, 2757.

Wallace, W.J. and Silsbee, R.H. (1991). *Review of Scientific Instruments*, **62**, 1754.

Wigen, P.E., Roukes, M.L. and Hammel, P.C. (2006). In *Spin Dynamics in Confined Magnetic Structures III*, *Vol. 101/2006 of Topics in Applied Physics*, Hillebrands, B. and Thiaville, A. (Eds.), Springer-Verlag: Berlin, Heidelberg, pp. 105–136, Chapter 3.

Yannoni, C.S., Züger, O., Rugar, D. and Sidles, J.A. 1996). In *Encyclopedia of Nuclear Magnetic Resonance*, Grant, D.M. and Harris, R.K. (Eds.), Wiley: Chichester, pp. 2093–2100.

Yu, X-M., Jiang, X-L., Thaysen, J., *et al*. (2001). Noise and sensitivity in polysilicon piezoresistive cantilevers. *Chinese Physics*, **10**, 918.

Zhang, Y. and Blencowe, M.P. (2001). Intrinsic noise of a micromechanical displacement detector based on the radio-frequency single-electron transistor. *Journal of Applied Physics*, **91**, 4249.

Zhang, Z. and Hammel, P.C. (1999). *Solid State Nuclear Magnetic Resonance*, **11**, 65.

Zhang, Z., Hammel, P.C., Midzor, M., *et al*. (1998). Ferromagnetic resonance force microscopy on microscopic cobalt single layer films. *Applied Physics Letters*, **73**, 2036.

Zhang, Z., Hammel, P.C. and Wigen, P.E. (1996). Sensitivity and spatial resolution for electron-spin-resonance detection by magnetic resonance force microscopy. *Applied Physics Letters*, **68**, 2005.

Zhang, Z., Roukes, M.L. and Hammel, P.C. (1996). *Journal of Applied Physics*, **80**, 6931.